Epigenomic Diversity of Cortical Projection Neurons in the Mouse Brain

Zhuzhu Zhang[1*], Jingtian Zhou[1,2*], Pengcheng Tan[1,3], Yan Pang[4], Angeline Rivkin[1], Megan A. Kirchgessner[4,5], Elora Williams[6], Cheng-Ta Lee[7], Hanqing Liu[1,8], Alexis D. Franklin[4], Paula Assakura Miyazaki[4], Anna Bartlett[1], Andrew Aldridge[1], Minh Vu[4], Lara Boggeman[9], Conor Fitzpatrick[9], Joseph R. Nery[1], Rosa G. Castanon[1], Mohammad Rashid[4], Matthew Jacobs[4], Tony Ito[4], Bertha Dominguez[7], Sheng-Yong Niu[1], Jared B. Smith[6], Carolyn O'Connor[9], Kuo-Fen Lee[7], Xin Jin[6], Eran A. Mukamel[10], M. Margarita Behrens[11], Joseph R. Ecker[1,12†], and Edward M. Callaway[4†]

[1]Genomic Analysis Laboratory, The Salk Institute for Biological Studies, La Jolla, CA 92037

[2]Bioinformatics and Systems Biology Program, University of California San Diego, La Jolla, CA 92093

[3]School of Pharmaceutical Sciences, Tsinghua University, Beijing, China, 100084

[4]Systems Neurobiology Laboratories, The Salk Institute for Biological Studies, La Jolla, CA 92037

[5]Neurosciences Graduate Program, University of California, San Diego, La Jolla, CA 92093

[6]Molecular Neurobiology Laboratory, The Salk Institute for Biological Studies, La Jolla, CA 92037

[7]Peptide Biology Laboratories, The Salk Institute for Biological Studies, La Jolla, CA 92037

[8]Division of Biological Sciences, University of California San Diego, La Jolla, CA 92093

[9]Flow Cytometry Core Facility, The Salk Institute for Biological Studies, La Jolla, CA 92037

[10]Department of Cognitive Science, University of California, San Diego, La Jolla, CA 92037

[11]Computational Neurobiology Laboratory, The Salk Institute for Biological Studies, La Jolla, CA 92037

[12]Howard Hughes Medical Institute, The Salk Institute for Biological Studies, La Jolla, CA 92037

[†]Correspondence: callaway@salk.edu, ecker@salk.edu

*These authors contributed equally

Summary

Neuronal cell types are classically defined by their molecular properties, anatomy, and functions. While recent advances in single-cell genomics have led to high-resolution molecular characterization of cell type diversity in the brain, neuronal cell types are often studied out of the context of their anatomical properties. To better understand the relationship between molecular and anatomical features defining cortical neurons, we combined retrograde labeling with single-nucleus DNA methylation sequencing to link epigenomic properties of cell types to neuronal projections. We examined 11,827 single neocortical neurons from 63 cortico-cortical (CC) and cortico-subcortical long-distance projections. Our results revealed unique epigenetic signatures of projection neurons that correspond to their laminar and regional location and projection patterns. Based on their epigenomes, intra-telencephalic (IT) cells projecting to different cortical targets could be further distinguished, and some layer 5 neurons projecting to extra-telencephalic targets (L5-ET) formed separate subclusters that aligned with their axonal projections. Such separation varied between cortical areas, suggesting area-specific differences in L5-ET subtypes, which were further validated by anatomical studies. Interestingly, a population of CC projection neurons clustered with L5-ET rather than IT neurons, suggesting a population of L5-ET cortical neurons projecting to both targets (L5-ET+CC). We verified the existence of these neurons by labeling the axon terminals of CC projection neurons and observed clear labeling in ET targets including thalamus, superior colliculus, and pons. These findings highlight the power of single-cell epigenomic approaches to connect the molecular properties of neurons with their anatomical and projection properties.

46 **Main Text**

47 The mammalian brain is a complex system consisting of multiple types of neurons with diverse
48 morphology, physiology, connections, gene expression, and epigenetic modifications. Identifying
49 brain cell types and how they interact is critical to understanding the neural mechanisms that
50 underlie brain function. During the last decade, these efforts have been facilitated by the advent of
51 molecular, genetic and viral tools for allowing genetic access and manipulation of specific cell
52 types[1,2]. Available evidence suggests, however, that there are far more cell types than can presently
53 be accessed genetically. Moreover, the correspondence between molecular cell types and neuronal
54 populations defined by connectivity are largely unknown.

55

56 Single-cell technologies deconvolve mammalian brains into molecularly defined cell clusters
57 corresponding to putative neuron types[3]. Among these technologies, single nucleus methylation
58 sequencing (snmC-Seq) applied to neurons has the unique ability to allow identification of
59 potential regulatory elements and a prediction of gene expression in the same cells. This is because
60 methylation at non-CG (CH; H= A, T, C) dinucleotides (mCH) of the gene body is inversely
61 correlated with RNA expression, and methylation at both CG dinucleotides (mCG) and CH
62 dinucleotides can be used to identify gene regulatory elements associated with gene expression[4–
63 6]. Furthermore, CH methylation accumulates and CG methylation reconfigures during cortical
64 synaptic development, suggesting possible links between epigenetics and connectivity[7,8].

65

66 Previous single-cell analyses have revealed transcriptomic clusters and linked them to neuron
67 types with different projection patterns in a few particular brain regions[9–12]. For the cerebral cortex,
68 the most prominent molecular distinction related to projection targets is the separation of cortical

69 neurons into distinct and apparently non-overlapping IT and L5-ET (also called pyramidal tract,
70 PT) groups. In some cases L5-ET cells have been further divided based on both gene expression
71 and corresponding axon projections[9]. While the separation of L5-IT and ET neurons appears to be
72 conserved across cortical areas[13] and species[14], a systematic analysis of the relationships between
73 a larger set of projection targets and molecular identities across multiple cortical areas has not been
74 conducted. To what extent cortical projection neuron types can be further distinguished or divided
75 by incorporating anatomical information with molecular analyses, and whether these cell types
76 and correspondences are conserved across cortical areas is unclear. Ultimately, the use of methods
77 that can classify cell types and predict regulatory elements, such as snmC-seq, will be critical to
78 understanding cell type and/or projection type specific regulatory mechanisms.
79
80 To address these questions we developed Epi-Retro-Seq, which applies snmC-Seq[15] to neurons
81 dissected from cortical source regions which were labeled based on their long distance projections
82 to specific cortical and subcortical targets. We analyzed the methylomes of 11,827 single neurons
83 from eight cortical areas projecting to ten target regions. This dataset enabled us to quantify the
84 epigenetic differences between cortical projection neurons, to identify specific genes and
85 regulatory elements in projection neurons, to study the relationships between cortical projection
86 neurons and molecular cell types, and to identify a neuron type making projections to both cortical
87 and ET targets.
88

Results

Epi-Retro-Seq of 63 cortical projections

To obtain a comprehensive view of the molecular diversity among cortical projection neurons we performed Epi-Retro-Seq, which combines retrograde tracing with epigenomic profiling. We characterized projection neurons from eight cortical areas ("source") spanning the anterior-to-posterior extent of the mouse cortex that project to ten cortical or subcortical regions ("target") (Fig. 1a), covering overall 26 CC projections and 37 cortico-subcortical projections (Supplementary Table 1). In Epi-Retro-Seq, the retrograde viral tracer rAAV2-retro-Cre is injected in the target region in an INTACT mouse[4], turning on Cre-dependent nuclear-GFP expression in neurons that project to the injected target, throughout the mouse brain. The brain is then sectioned into eighteen 600-micron coronal slices, and the source regions of interest are dissected from each slice (see Methods). Nuclei are sampled from at least 4 mice (2 male and 2 female) for each projection target (except AI→pons - 2 male mice only). Nuclei from each of the dissected source regions are prepared, from which $GFP^+/NeuN^+$ nuclei (the GFP-labeled projection neurons) are isolated as single nuclei using fluorescence activated nuclei sorting (FANS) and assayed using snmC-Seq2[15] to profile their genome-wide DNA methylation signatures. The ten injected target regions include four cortical areas [the primary motor cortex (MOp), primary somatosensory cortex (SSp), anterior cingulate area (ACA), and primary visual cortex (VISp)], and six major subcortical structures [the striatum (STR), thalamus (TH), superior colliculus (SC), ventral tegmental area and substantia nigra (VTA+SN), pons, and medulla (MY)]. Each of the eight source cortical regions [MOp, SSp, ACA, agranular insular cortex (AI), retrosplenial cortex (RSP), auditory cortex (AUDp+AUDd+AUDv), posterior parietal cortex (PTLp), and visual cortex (VISp+VISpm+VISl+VISli)] were hand dissected from one or two coronal slices following the

112 Allen Mouse Common Coordinate Framework (CCF), Reference Atlas, Version 3 (2015)
113 (Extended Data Fig. 1).
114
115 **Methylation landscape of cortical projection neurons**
116 We assayed approximately 384 nuclei from each projection (except the MOp→SSp projection
117 from which 768 nuclei were assayed). After removing the low-quality cells, potential doublets,
118 and glial cells (possibly due to false NeuN positives in FANS), we obtained high-quality single
119 methylomes for 11,827 cortical projection neurons (Extended Data Fig. 2). The level of CH
120 methylation in each single nucleus was computed across the genome using 100 kb genomic bins
121 and used to perform unsupervised clustering of the projection neurons. Overall, the cortical
122 projection neuron clusters were annotated into 10 major cell types (Fig. 1b) based on the reduced
123 levels of gene body mCH, a proxy for gene expression, of known marker genes (Extended Data
124 Fig. 2f). It should be noted that 361 neurons (3.05%) fell into the inhibitory neuron cluster, likely
125 representing false-positives possibly, due to either labeling of neurons by AAV that leaked into
126 cortical areas above subcortical injection sites (mostly from areas above TH injections), or
127 insufficient gating stringency during FANS, allowing inclusion of GFP-negative nuclei. This low
128 error rate allows a rough estimate of the likely erroneous contributions from other cell types.
129 Within each cell type cluster, excitatory neurons but not inhibitory neurons from different cortical
130 regions were further separated from each other (Fig. 1c), demonstrating that such separations in
131 excitatory neuron clusters were not due to technical effects but instead represented the distinct
132 spatial DNA methylation patterns in cortical projection neurons. As can be seen from the t-SNE
133 visualization (Fig. 1d), neurons projecting to different target regions were more similar within each
134 cluster than neurons from different source regions, indicating that they shared a more similar DNA

135 methylation landscape. Neighbor enrichment scores were used to quantify the variations of DNA
136 methylation that originated from different cell types, cortical spatial regions, and projection targets
137 (see Methods). Neurons from the same cluster occupied highly similar regions in the dimension
138 reduction space (neighbor enrichment score was near 1). Scores were also high for comparisons
139 across neurons from the same source, followed by projections to the same target. Scores were near
140 chance for biological replicates (Fig. 1h).
141
142 Next, we integrated our data with the single-nuclei methylation data that were dissected and
143 sorted from some of the same cortical regions but without enrichment of specific projections (Liu
144 et al., companion paper #9). We observed a close agreement of the major cell types (Fig. 1e) and
145 source regions (Fig. 1f) between these two datasets. Given the increased number of cells, different
146 source regions became better demarcated on t-SNE (Fig. 1f). Compared with unbiased snmC-seq2
147 profiling, Epi-Retro-seq dataset also contains information about the neuronal projection targets
148 revealed by retrograde tracing (Fig. 1g). This enabled enrichment of rare types of projection
149 neurons and analysis of the methylation patterns of neurons projecting to different brain regions.
150
151 Although neurons projecting to different target regions were not completely separated on t-SNE,
152 we observed an explicit enrichment of CC and cortico-striatal projection neurons in IT clusters
153 (L2/3, L4, L5-IT, L6-IT, and Claustrum (CLA)), separated from neurons that project to the
154 remaining structures outside the telencephalon which were categorized as L5-ET neurons (Fig. 1j,
155 Extended Data Fig. 3) As expected, many cortico-thalamic projecting neurons were also found in
156 the L6-CT cluster (Fig. 1j, Extended Data Fig. 3). These enrichment patterns are consistent with

157 our knowledge about laminar enrichment of the projection neurons, which reflects the high quality
158 of our retrogradely labeled single-nuclei methylation dataset.
159
160 To further quantify methylation differences between neurons from different source regions or
161 projecting to different target regions, we made comparisons across source pairs or target pairs. For
162 each pair of interest, area under the curve of receiver operating characteristic (AUROC) was
163 calculated to score the level of separation between the two groups of projection neurons.
164 Specifically, a logistic regression model was trained using normalized gene body mCH as features
165 to predict which group a cell belongs to. By training the model in one biological replicate and
166 testing on the other, the performance was measured by AUROC. By comparing each pair of
167 sources or targets, we found that most neurons dissected from different source regions could be
168 separated with AUROC > 0.9 (Fig. 1i). Most of the neurons projecting to different target regions
169 were also separable by mCH in this supervised setting (Fig. 1i), although they were closely mixed
170 in the unsupervised embeddings (Fig. 1d). These findings indicate that nearly all of the different
171 types of projection neurons that were profiled have differences in their epigenomes.
172
173 **Epigenetic diversity of IT neurons projecting to different cortical targets**
174 As described above, assessment of the entire Epi-Retro-Seq dataset revealed clear and expected
175 differences in the neuron clusters occupied by neurons projecting to IT versus ET targets, and these
176 differences were conserved across source areas. However, neurons projecting to different IT or ET
177 targets did not uniquely separate into distinct clusters when analyzed at the level of the entire cell
178 population. Nevertheless, we were able to detect projection-dependent quantitative differences in

179 the levels of DNA methylation. Further analyses of these quantitative differences, described below,
180 allowed assessment of possible organizational principles that might exist in the relationships
181 between DNA methylation, projections targets, and sources, including both areal and laminar
182 sources.
183
184 In total, 42.6% of the cortical projection neurons profiled in our Epi-Retro-Seq data were
185 identified as IT, and annotated according to their presumptive cortical layers (Fig. 1b). We next
186 aimed to disentangle the contribution of the cortical area in which cell bodies were located versus
187 their cortical projection targets, to the variation of their DNA methylation profiles. We focused on
188 26 CC projections from 8 cortical areas to 4 different cortical targets. AUROC scores were used
189 to evaluate epigenetic relationships between cortical neurons projecting to different cortical targets.
190 All possible pairs of 4 cortical targets were assessed for each of the 8 sources to generate 29
191 AUROC scores, organized according to projection target pairs (Fig. 2a, Extended Data Fig. 4a, c).
192 Significant differences were observed between projection target pairs when assessed across source
193 areas (p=6.8e-3, Kruskal-Wallis test), but not between cortical areas when assessed across target
194 pairs (p=0.3, Kruskal-Wallis test). Among the six projection target pairs examined, neurons
195 projecting to MOp versus ACA were overall most distinguishable (average AUROC = 0.902),
196 followed by neurons projecting to ACA versus VISp (average AUROC = 0.887), while neurons
197 that project to SSp versus ACA were the least separable (average AUROC = 0.693) (Fig. 2a). In
198 addition, for each target pair, the performance of the predictive model varied among neurons from
199 different source cortical regions (Fig. 2a, Extended Data Fig. 4a, c).
200

201 Together, these analyses suggest that epigenetic differences between CC projection neurons
202 depend on a combination of both the specific targets to which neurons project and the source region
203 where the neurons reside. For example, we further evaluated the variability of mCH profiles among
204 AUD IT neurons projecting to different targets and found that AUD→SSp neurons were better
205 separated from AUD→VISp neurons (AUROC = 0.94; Fig.2b, e) than from AUD→ACA neurons
206 (AUROC = 0.709; Fig. 2c, e). t-SNE plots color-coded according to these same projection
207 comparisons (Fig. 2b, c) or according to annotated layers (Fig. 2d) allow visualization of the extent
208 to which these neurons differ. In addition to the apparent greater separability of AUD→SSP versus
209 AUD→VISp than AUD→SSP versus AUD→ACA neurons, it can be seen that the distinctions
210 between these projections did not stem from different distributions across layers (Fig. 2d). This
211 demonstrates that the level of epigenetic differences between AUD IT neurons varies depending
212 on their projection targets. On the other hand, when comparing neurons from different sources
213 projecting to the same target pair, we observed different levels of distinguishability in our models.
214 For example, while MOp-projecting versus ACA-projecting neurons were more distinguishable
215 (i.e. higher AUROC scores) than SSp-projecting versus ACA-projecting neurons, we observed
216 variation of the AUROC scores across different source regions for both target pairs (Fig. 2f, g).
217
218 To further validate that the differences in separability across regions resulted from biological
219 differences rather than limited sample sizes for some regions, we trained our predictive model
220 between two targets using neurons from one source region and then tested the performance of the
221 model on another source region. These analyses also allowed evaluation of whether the same
222 epigenetic differences that distinguished target pairs for one source area might be conserved across
223 source areas. As expected, the performances of the cross-source-region models in distinguishing

two projection targets were usually less than the same-source-region models (Fig. 2h, i, Extended Data Fig. 4b, d). Nevertheless, many target pairs that were distinguishable for the within-source models were also distinguishable with the cross-source models (Fig. 2h, i, Extended Data Fig. 4b, d), indicating conservation of target pair epigenetic differences across sources. Interestingly, the performance of models trained on any particular region varied in their ability to predict projections from other regions. For example, the model trained on data from AUD performed better in distinguishing VIS→MOp versus VIS→ACA neurons than the models trained on RSP, PTLp, or SSp (Fig. 2h). This suggests that AUD and VIS neurons are more similar to each other in the molecular markers that distinguish neurons projecting to MOp versus ACA than other cortical areas. These results indicate that cortical regions might form different groups with shared correlations between molecular markers and projection targets.

In addition, the level of distinguishability between two cortical targets appeared to be similar across layers (Fig. 2j, Extended Data Fig. 5a, b). By training and testing the predictive models in each layer separately, we observed higher distinguishability between ACA-projecting versus VISp-projecting neurons across all layers than between SSp-projecting versus ACA-projecting in all layers in almost all source regions (Fig. 2j, k). We further tested if cross-layer-trained models could distinguish the projection targets (see Methods), and observed that the performance was generally comparable to within-layer models (Extended Data Fig. 5c, d). These results suggest that there may be shared epigenetic signatures across layers that contribute to correlations with the projection targets.

246 To better understand the biology underlying the epigenetic signatures that distinguish different
247 cortical IT projection neurons, we identified differentially methylated genes at CH sites (CH-
248 DMGs) between different pairs of CC projection neurons in each source region using hierarchical
249 linear models. In total, 1830 CH-DMGs were identified (Supplementary Table 3), among which
250 1,623 (88.7%) were statistically significant in only one source region, and 207 (11.3%) were
251 differentially methylated in more than one source region (some examples shown in Fig. 2l). That
252 the vast majority of CH-DMGs were unique to one source region, suggests that different genes
253 may participate in defining projections from different source regions. Gene ontology (GO)
254 enrichment analysis revealed that CH-DMGs were enriched for genes that participate in
255 intracellular transport, regulation of synapse structure, etc. (Fig. 2m), all relevant for influencing
256 neuronal projections. For example, Bassoon (*Bsn*) is differentially methylated between MOp-
257 projecting and SSp-projecting neurons in ACA, AUD, and VIS (Fig. 2l). It encodes a presynaptic
258 cytomatrix protein expressed primarily in neurons, and is essential in regulation of
259 neurotransmitter release[16]. *Scn2a1* encodes a voltage dependent sodium channel protein and is
260 differentially methylated between SSp-projecting and VISp-projecting neurons in ACA, AI, AUD,
261 and PTLp (Fig. 2l). This channel regulates neuronal excitability and variants are associated with
262 autism and seizure disorders[17].
263

264 **Epigenetically distinct subpopulations of L5-ET neurons**

265 In our Epi-Retro-Seq data, 5 out of the 10 profiled projection targets are ET. In particular, L5-ET
266 neurons are the most abundant cell population in our datasets (4,176 (35.3%) single neurons), and
267 are 6.3 fold enriched in Epi-Retro-Seq compared to the total number of neurons observed in
268 unbiased snmC-seq2 profiling. This level of L5-ET neuron enrichment provides us with a unique

269 opportunity to more closely investigate subpopulations of L5-ET neurons. In unsupervised
270 clustering using genome-wide mCH levels measured in 100 kb genomic bins, L5-ET neurons
271 further segregated into 15 subclusters upon uniform manifold approximation and projection
272 (UMAP) embedding (Fig. 3a). Much of the separation between subclusters was driven by the
273 source location of the neurons, as neurons from different source regions were clearly separated on
274 the UMAP (Fig. 3b) and each of the subclusters consists of neurons mostly from one or two source
275 regions (Extended Data Fig. 6a). In particular, RSP and AI each formed their own specific
276 subcluster (cluster 13 and 3, respectively; Extended Data Fig. 6a, b). The similarities and
277 differences between L5-ET neurons from different source regions were quantified using
278 hierarchical clustering (Fig. 3c). The genome-wide mCH similarity is highest between MOp and
279 SSp, followed by between VIS and AUD, and between PTLp and ACA. AI and RSP were more
280 distinct; in particular, RSP was well separated from the remaining cortical regions. These
281 similarities between source regions were not well explained by their spatial proximity anterior-
282 posteriorly or medial-laterally, but better correlated with the anatomical and functional
283 connectivity between these regions. For example, MOp and SSp are components of the somatic
284 sensorimotor subnetwork, while AUD, VIS, ACA, and PTLp are components of the medial
285 subnetwork that channels information between sensory areas (that include VISp and AUD) and
286 higher order association areas (that include PTLp and ACA)[18].
287
288 To further explore the molecular identity of these L5-ET subclusters, we used gene body mCH
289 levels to identify cluster-specific genes. In total 2,675 CH-DMGs were identified in pairwise
290 comparisons between subclusters (Fig. 3d, Supplementary Table 4; examples in Extended Data
291 Fig. 6c), indicating that these genes have cluster-specific expression patterns. Gene ontology (GO)

292 enrichment analysis revealed that these L5-ET subcluster CH-DMGs were enriched in genes
293 involved in cell communication, neurogenesis, cell morphogenesis, and axon guidance (Fig. 3e,
294 Supplementary Table 4).
295
296 In addition to identification of cluster-specific gene markers using gene body mCH, a powerful
297 and unique advantage of methylation profiling is that cis-elements that regulate the marker genes
298 can be predicted based on CG methylation. Differentially CG methylated regions (CG-DMRs)
299 between clusters reliably mark cis-regulatory elements across the whole genome (not limited to
300 gene bodies). Here, we identified 341,748 CG-DMRs that were hypo-methylated in the
301 corresponding L5-ET subclusters (Fig. 3f, Supplementary Table 5). The average length of CG-
302 DMRs was 227 bp, and 84.9% of them were distal elements that located more than 5kb from the
303 annotated transcription start sites (TSSs).
304
305 The level of mCH at gene bodies is inversely correlated with gene expression, while the level of
306 mCG at gene regulatory elements, such as promoters and enhancers, is inversely correlated with
307 their regulatory activities. These relationships allowed us to use a gene regulatory network-based
308 method to integrate this information and identify transcription factors (TFs) that might function as
309 key regulators in each subcluster (see Methods; Fig. 3g). Specifically, in this network the nodes
310 were genes (including TFs), while the edges connected the TFs to their potential target genes based
311 on the TF binding motifs in CG-DMRs surrounding the TSSs. The weights of the nodes and edges
312 were set according to the predicted expression levels (gene body mCH) of the genes. After
313 applying a PageRank algorithm to score the genes in the network, we identified TFs that were
314 potentially highly expressed and may regulate many other highly expressed genes in a subset of

315 L5-ET clusters. This method combined the advantages of differential expression and motif
316 enrichment analysis (Extended Data Fig. 6d, e), and enabled us to find TFs that may be expressed
317 among a family of TFs sharing similar motifs[19]. For example, *Rora* (RAR Related Orphan
318 Receptor A), a transcriptional activator, was scored as one of the top TFs and is hypo-CH-
319 methylated in clusters 1, 8, and 13, and especially in cluster 8 (Fig. 3h, Extended Data Fig. 6d),
320 indicating its potential expression. The binding motif of RORA was also enriched in the CG-DMRs
321 of these same clusters, suggesting that RORA may bind to cis-regulatory elements that in turn
322 regulate a set of predicted downstream target genes. Many of these target genes are related to brain
323 functions and also hypo-methylated in cluster 8 (Extended Data Fig. 6f). For example, one of its
324 predicted downstream target genes, *Astn1* (Astrotactin 1) is also hypo-CH-methylated in cluster 8
325 and encodes for a neuronal adhesion molecule, showing clear correlation between *Rora* and *Astn1*
326 expression inferred from gene-body mCH (Fig. 3i).
327
328 **Subclusters of L5-ET neurons project to different targets**
329 Our analyses of cortical IT neurons revealed epigenetic differences between neurons that related
330 to both their cortical locations and their projection targets. Although the separation of L5-ET
331 neuron subclusters was mostly driven by the source regions, neurons from the same source regions
332 (except AI and RSP) distributed into more than one subcluster (Fig. 3a, b Extended Data Fig. 6b),
333 prompting us to ask whether some of the differences between L5-ET subclusters also correspond
334 to the different projection targets. To investigate this, we performed another iteration of clustering
335 analysis using L5-ET cell data from each of the source regions separately, and identified finer L5-
336 ET subclusters within each source region (Extended Data Fig. 7a). Consistent with these
337 subclusters being related to true differences between putative cell types, all pairs of subclusters

338 had more than 5 differentially CH-methylated 100 kb bins (CH-DMBs) (298 CH-DMBs on
339 average).
340
341 We then examined whether neurons projecting to a specific target region were enriched or
342 depleted in any of the subclusters (Extended Data Fig. 7c, d). Among all comparisons between
343 projection targets and subclusters, neurons projecting to medulla (MY) were most distinct. SSp
344 L5-ET neurons further segregated into seven subclusters (Fig. 4a), among which SSp→MY
345 neurons showed a clear enrichment in subcluster 0 (FDR = 1.72E-2, Wald test; Fig. 4b, c).
346 Similarly, we identified seven subclusters of MOp L5-ET neurons, and MOp→MY neurons were
347 also significantly enriched in one of the subclusters (FDR = 6.81E-3, Wald test; Extended Data
348 Fig. 7c, d). Moreover, MY-projecting neurons were robustly distinguished from other L5-ET
349 neurons in our prediction models for both MOp and SSp (average AUROC = 0.929, 0.860; Fig.
350 4d, Extended Data Fig. 8a). Together, these analyses suggest that MY-projecting L5-ET neurons
351 are more distinct than L5-ET neurons projecting to the other targets that were assessed.
352
353 To investigate which genes drive the observed epigenomic differences between MY-projecting
354 L5-ET neurons and other L5-ET neurons, we compared the gene body CH methylation profiles of
355 MY-projecting L5-ET neurons to L5-ET neurons projecting to each of the other ET targets. In
356 total, we identified 1,380 CH-DMGs between MOp→MY L5-ET neurons and at least one of the
357 other ET projections (Fig. 4e, Supplementary Table 6). The majority of CH-DMGs were shared
358 across the other ET projections. Specifically, among the 939 CH-DMGs that were hypo-
359 methylated in MY-projecting neurons, 98 (10.4%) were universally hyper-methylated in all the
360 other ET projections; Among the 441 CH-DMGs that were hyper-methylated in MY-projecting

361 neurons, 85 (19.3%) were hypo-methylated in all the other ET projections. These results suggest
362 that there are shared molecular differences that distinguish MOp→MY neurons from MOp
363 neurons that project to VTA, SC, Pons, or TH. Similarly, 285 CH-DMGs were identified between
364 SSp→MY L5-ET neurons and at least one of the other ET projections (Fig. 4f, Supplementary
365 Table 6), among them 111 were hypo-methylated in SSp→MY neurons and 174 were hyper-
366 methylated.
367
368 In total, 171 CH-DMGs were identified in both MOp→MY and SSp→MY neurons (a few
369 examples highlighted in Fig. 4e, f), suggesting a general regulatory mechanism that may be shared
370 by different cortical regions. Accordingly, models trained in either MOp or SSp to distinguish
371 MY-projecting neurons usually performed well when tested in the other region (Extended Data
372 Fig. 8b). Indeed, similar enrichment of MY-projecting neurons in subpopulations of L5-ET
373 neurons has been reported in ALM using scRNA-seq (retro-seq)[13]. To compare these observations,
374 we used gene body mCH as a proxy for gene expression to integrate our L5-ET Epi-Retro-Seq
375 data with the ALM retro-seq data. Joint t-SNE showed that the MY-projecting L5-ET neurons
376 were enriched in the same subcluster (Extended Data Fig. 9). *Slco2a1*, a marker gene of the ALM
377 MY-projecting cluster[9,13] is hypo-methylated in MOp→MY but not in SSp→MY neurons
378 (Extended Data Fig. 9h). We identified *Astn2* as a marker gene for the MY-projecting L5-ET
379 cluster in both MOp and SSp (Extended Data Fig. 9i). ASTN2 mediates the recycling of neuronal
380 cell adhesion molecule ASTN1 in migrating neurons, and its deletion has been associated with
381 schizophrenia. This suggests that, compared to other L5-ET neurons, MY-projecting neurons have
382 distinct molecular properties, and these distinctions are likely shared across several cortical regions.
383

384 In addition to the MY-projecting L5-ET neurons, we also observed differences in genome-wide
385 mCH profiles between other ET projections. For example, L5-ET neurons in AI were segregated
386 into five subclusters (Fig. 4g), and AI→Pons and AI→SC neurons were enriched in different
387 subclusters (Fig. 4h, i, Extended Data Fig. 8c). In contrast, AI→Pons and AI→TH neurons were
388 enriched in similar subclusters (Extended Data Fig. 8c). Analysis of gene body mCH identified
389 145 CH-DMGs that were differentially methylated between AI→SC neurons versus AI→Pons,
390 while most of them had similar expression patterns between AI→Pons and AI→TH neurons (Fig.
391 4j). Together, the results suggest that AI→Pons neurons are more distinct from AI→SC neurons
392 and are similar to AI→TH neurons.
393
394 In contrast to the conservation across cortical areas ALM, MOp, and SSp for differences related
395 to projections to MY, differences between Pons-projecting and SC-projecting neurons were not
396 conserved across all cortical areas. We trained a prediction model using mCH profiles to
397 distinguish Pons- versus SC-projecting neurons from different source regions. The model
398 performed well in distinguishing the two projections from cortical regions AI (AUROC = 0.939)
399 and VIS (AUROC = 0.868), but performed poorly in PTLp neurons (AUROC = 0.726) (Extended
400 Data Fig. 8a). The AUROC scores were correlated with the counts of CH-DMGs identified
401 between SC-projecting versus Pons-projecting neurons in the corresponding source regions
402 (Spearman r=0.683). This suggests that the differences between Pons-projecting and SC-projecting
403 neurons vary across the cortex.
404
405 From these observations, we hypothesized that the level of the epigenetic differences between
406 the two projections might be correlated with the percentage of neurons that simultaneously project

407 to both Pons and SC, which might vary between different cortical regions. That is, in a cortical
408 area where more neurons project to both Pons and SC, the epigenetic profiles of Pons- and SC-
409 projecting neurons might be expected to be less distinguishable in our data, and vice versa. To test
410 this hypothesis, we performed double retrograde labeling of Pons and SC, and counted in each
411 cortical source region the number of neurons labeled only by the tracer injected into Pons, only
412 SC, or both (Supplementary Table 7). As our hypothesis predicted, PTLp had the highest
413 percentage of double-labeled neurons, and in general the AUROC score from our model was
414 negatively correlated with the percentage of double-labeled cells (Spearman r=-0.829, p=0.04)
415 across the cortical regions (Fig. 4k). These correspondences are weak, however, for most source
416 regions, so the correlation is driven primarily by the data from PTLp.
417
418 **L5-ET+CC neurons**
419 Intriguingly, we noticed more than 30 VISp-projecting neurons in L5-ET clusters from ACA and
420 RSP datasets (Fig. 5a, b). Since neurons in the L5-ET cluster are likely to project to ET targets,
421 this finding suggested that some L5 neurons might project to both cortical and ET targets. These
422 neurons were enriched specifically in one subcluster in ACA and RSP, respectively (FDR = 9.82E-
423 5, 2.45E-3, Wald test; Fig. 5a-d). This type of subcluster in both RSP and ACA was marked by
424 *Ubn2*, a highly expressed gene in visual systems, and many other genes also distinguished this
425 cluster in either region.
426
427 Although, ET cells are generally thought to lack projections to other cortical areas, there is some
428 evidence for such cells from previous studies[20]. Reconstructions of the axonal arbors of 24, L5
429 MOp neurons in rats revealed 3 neurons projecting to both SSp and TH[21], and neurons in mouse

430 secondary motor cortex have been shown to project to both AUD and ET targets[22]. In primates,
431 single neurons projecting to both a cortical target, visual area MT, and a subcortical target, SC,
432 have been observed in layer 6 of VISp[23,24]. However, since ET neurons represent a small
433 percentage of primate neurons, these dual-projection neurons are extremely rare; they are also
434 located in layer 6 rather than layer 5 making it difficult to predict whether they might be genetically
435 more closely related to ET or to IT neurons, whether they might project to additional subcortical
436 targets, or whether they might be unique to primates.
437
438 To anatomically validate our findings for RSP→VISp ET neurons in mice, we injected
439 AAVretro-Cre in VISp and AAV-flex-GFP (Cre-dependent GFP) in RSP in three mice (Fig. 5e).
440 This resulted in labeling of the complete axonal and dendritic arbors of RSP→VISp neurons such
441 that their long-distance projections to locations other than VISp could be assessed. We observed
442 strong GFP labeling of axon terminals in subcortical ET regions, including TH, SC, and Pons, in
443 all three mice (Fig. 5f). These results indicate that single neurons in L5 of RSP can project
444 simultaneously to both cortical and subcortical, ET targets in mice. Because these cells genetically
445 cluster with L5-ET cells, we consider them a subtype of L5-ET cells that we refer to as L5-ET+CC.
446 We do not use the term L5-ET+IT because many L5-ET neurons are known to project to another
447 part of the telencephalon, the striatum.
448
449 **Discussion**
450 Here, we have quantitatively analyzed and compared the methylation of mouse cortical neurons
451 projecting to different cortical and subcortical target regions. We identified genes that were
452 differentially methylated between different cortical areas projecting to the same targets, as well as

453 between neurons in the same areas projecting to different targets. As expected from previous
454 studies identifying IT- and ET-projecting neurons as distinct populations, these populations were
455 also the most distinct in their gene methylation. We also identified differences between both IT
456 neurons projecting to different cortical areas and between L5-ET neurons projecting to different
457 ET targets. Cortical IT neurons projecting to different cortical targets were variable in the extent
458 of their epigenetic differences. Some pairs of cortical target areas were more distinct than others
459 and these epigenetic differences were often conserved across cortical sources areas. Differences
460 between projection target pairs were typically larger than differences between cortical source areas
461 for any given pair of projection targets.
462
463 Most distinct amongst the L5-ET neurons were those projecting to the medulla. This difference
464 has been described previously for neurons in cortical area ALM[9] and we find that this difference
465 is conserved across the additional cortical areas that we analyzed, including MOp and SSp. In
466 contrast, differences between L5-ET neurons projecting to SC versus pons were more distinct in
467 some cortical areas (e.g. AI) than in others (e.g. PTLp). Dual retrograde tracer injections into both
468 SC and pons revealed a corresponding difference in the proportions of double-labeled cells in
469 different cortical areas, consistent with the expectation that neurons projecting to just one target
470 can be different while those projecting to both targets cannot.
471
472 We found that a subpopulation of cortico-cortical RSP→VISp and ACA→VISp neurons
473 clustered with L5-ET cells, contrary to the expectation that L5-ET and IT cortico-cortical cells are
474 distinct populations. This suggested that some L5-ET cells might project to cortical targets and
475 this hypothesis was validated anatomically. Our anatomical experiments showed that RSP→VISp

476 cells do in fact project to many ET targets, including TH, SC and pons, and we refer to this cell
477 type as L5 ET+CC. Although we found CC projection neurons that clustered with L5-ET cells for
478 only two of the 26 CC projections that we sampled, there remain many other combinations that we
479 did not test. Furthermore, previous studies have described L5 ET+CC cells in primary and
480 secondary motor cortex[21,22]. It is therefore likely that future studies will reveal L5-ET+CC neurons
481 in additional cortical areas projecting to various combinations of ET and cortical targets.
482
483 Finally, this large-scale effort linking methylation status directly to projection targets of mouse
484 cortical neurons, allowed us to identify differences between projection cell types in TFs linked to
485 differentially methylated regions. These observations provide insight into genetic mechanisms that
486 might contribute to the differences in morphology and function of these cell types. As we have
487 illustrated, this large dataset also provides the opportunity to predict regulatory elements that might
488 be harnessed in future studies to target transgene expression to these cell types.
489

Figures

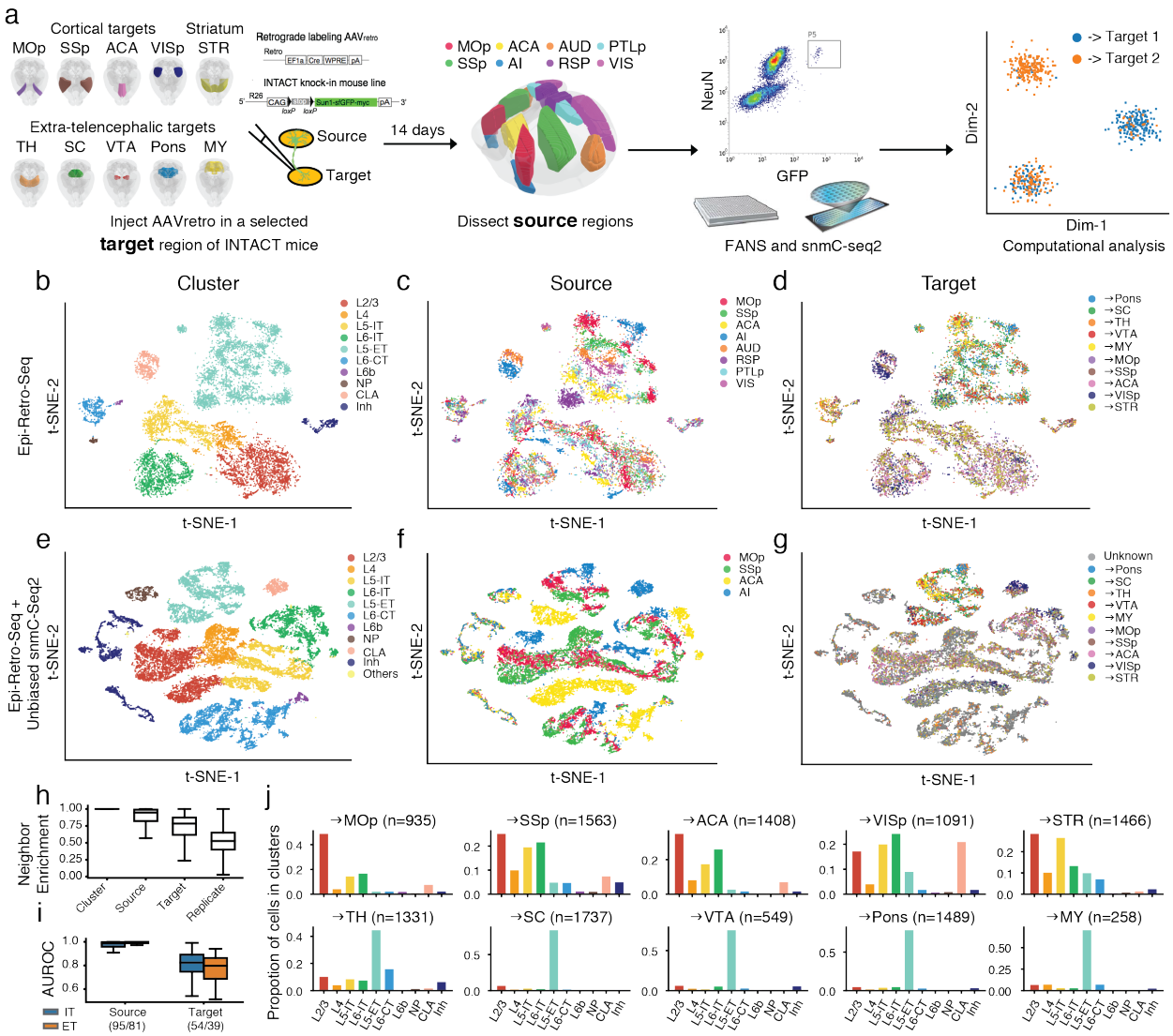

Fig. 1 The epigenomic landscape of cortical projection neurons.

a, Schematics of Epi-Retro-Seq workflow that retrogradely labels and epigenetically profiles single projection neurons. The retrograde tracer rAAV2-retro-cre was injected in one of the ten target regions (primary motor cortex (MOp), primary somatosensory cortex (SSp), anterior cingulate cortex (ACA), primary visual cortex (VISp), striatum (STR), thalamus (TH), superior colliculus (SC), the ventral tegmental area (VTA) & substantia nigra (SNr), Pons, or medulla (MY)) in INTACT knock-in mice. Therefore, nuclei of neurons that projected to the injected target

were labeled with cre-dependent nuclear GFP. Source regions of interest (MOp, SSp, ACA, agranular insular cortex (AI), auditory cortex (AUD), retrosplenial cortex (RSP), posterior parietal cortex (PTLp), or visual cortex (VIS)) were dissected 14 days after the injection, from which nuclei were prepared and single $GFP^+/NeuN^+$ nuclei were isolated using fluorescence activated nuclei sorting (FANS) followed by snmC-seq2 and computational analysis. Brain diagrams were derived from the Allen Mouse Brain Reference Atlas (version 3 (2015)). **b-d,** Two-dimensional t-distributed stochastic neighbor embedding (t-SNE) of 11,827 cortical neuron nuclei based on CH methylation (mCH) levels in 100 kb genomic bins, colored by cluster (**b**), the source region of neurons (**c**), or their projection target (**d**). Cortical neurons were better separated by their source regions than projection targets within each major cell type cluster. **e-g**, Integrative clustering of Epi-Retro-Seq and unbiased snmC-seq2 (without enrichment of projections) of neurons from MOp, SSp, ACA and AI (n=21,966), colored by cluster (**e**), source region (**f**), and projection targets in Epi-Retro-Seq (**g**). **h**, Neighbor enrichment scores of cells (n=11,827) categorized by cluster, source, target, and replicate. **i**, AUROC of source pairs and target pairs computed for IT (blue) and ET (orange) neurons based on gene body mCH. Sample sizes are shown in x-axis ticklabels. **j,** The distribution across cell clusters of neurons that projected to each IT (top row) or ET (bottom row) target. The elements of all boxplots are defined as: center line, median; box limits, first and third quartiles; whiskers, 1.5× interquartile range.

IT, intra-telencephalic; ET, extra-telencephalic; NP, near-projecting; CT, corticothalamic; Inh, inhibitory; CLA, claustrum; Others, cell clusters detected in unbiased snmC-seq2 but not in Epi-Retro-Seq.

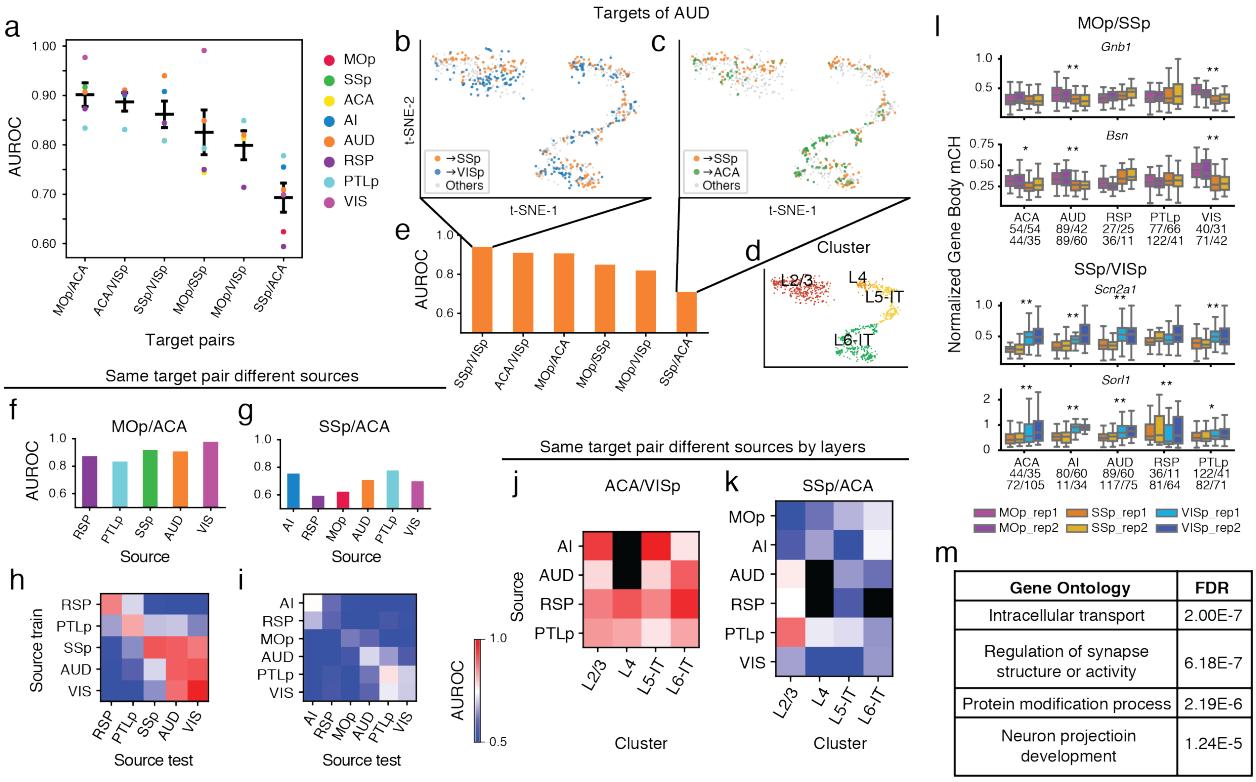

Gene Ontology	FDR
Intracellular transport	2.00E-7
Regulation of synapse structure or activity	6.18E-7
Protein modification process	2.19E-6
Neuron projectioin development	1.24E-5

Fig. 2 Epigenetic differences between IT neurons projecting to different targets.

a, AUROC from the prediction model constructed to distinguish cortical neurons projecting to one cortical target versus another was used to measure the epigenetic variation between different cortical IT neurons. A significant variation of AUROC among different projection target pairs was observed. **b-e**, Upon examining AUD IT neurons (n=737) that project to different cortical targets, AUD→SSp neurons and AUD→VISp neurons were biased toward different locations within each layer-annotated cluster (**d**) on the t-SNE plot using mCH levels in gene bodies (**b**), while AUD→SSp neurons and AUD→ACA neurons were more intermingled (**c**). The differential levels of separation on t-SNE corresponded to the high AUROC between AUD→SSp versus AUD→VISp neurons, and low AUROC between AUD→SSp versus AUD→ACA neurons (**e**). **f, g**, The AUROC for comparisons between →MOp versus →ACA neurons from different source regions varied between 0.834 and 0.977 (**f**), while the AUROC for comparisons between →SSp

versus →ACA neurons from different source regions varied between 0.594 and 0.778 (**g**), indicating overall higher levels of distinguishability between →MOp versus →ACA neurons, than between →SSp versus →ACA neurons. **h, i**, Heatmaps of AUROC from prediction models that were trained on one source region (row) and tested on another source region (column) to distinguish between neurons projecting to →MOp versus →ACA (**h**), or between →SSp versus →ACA neurons (**i**). **j, k**, Heatmaps of AUROC from prediction models that were trained and tested on neurons from each cortical layer (column) in each source region (row), to distinguish between →ACA versus →VISp neurons (**j**), or between →SSp versus →ACA neurons (**k**). **l**, Boxplots of example genes that were differentially methylated at CH sites (CH-DMGs) between →MOp versus →SSp neurons (top), or between →SSp versus →VISp neurons (bottom). The sample sizes are shown as ticklabels of x-axis. ** represents false discovery rate (FDR)<0.01 and * represents FDR<0.1. **m**, Gene ontology (GO) enrichment of 1,830 CH-DMGs between cortical neurons projecting to different cortical targets. The elements of all boxplots are defined as: center line, median; box limits, first and third quartiles; whiskers, 1.5× interquartile range. Center lines and error bars in (a) represent the means and standard errors of the means.

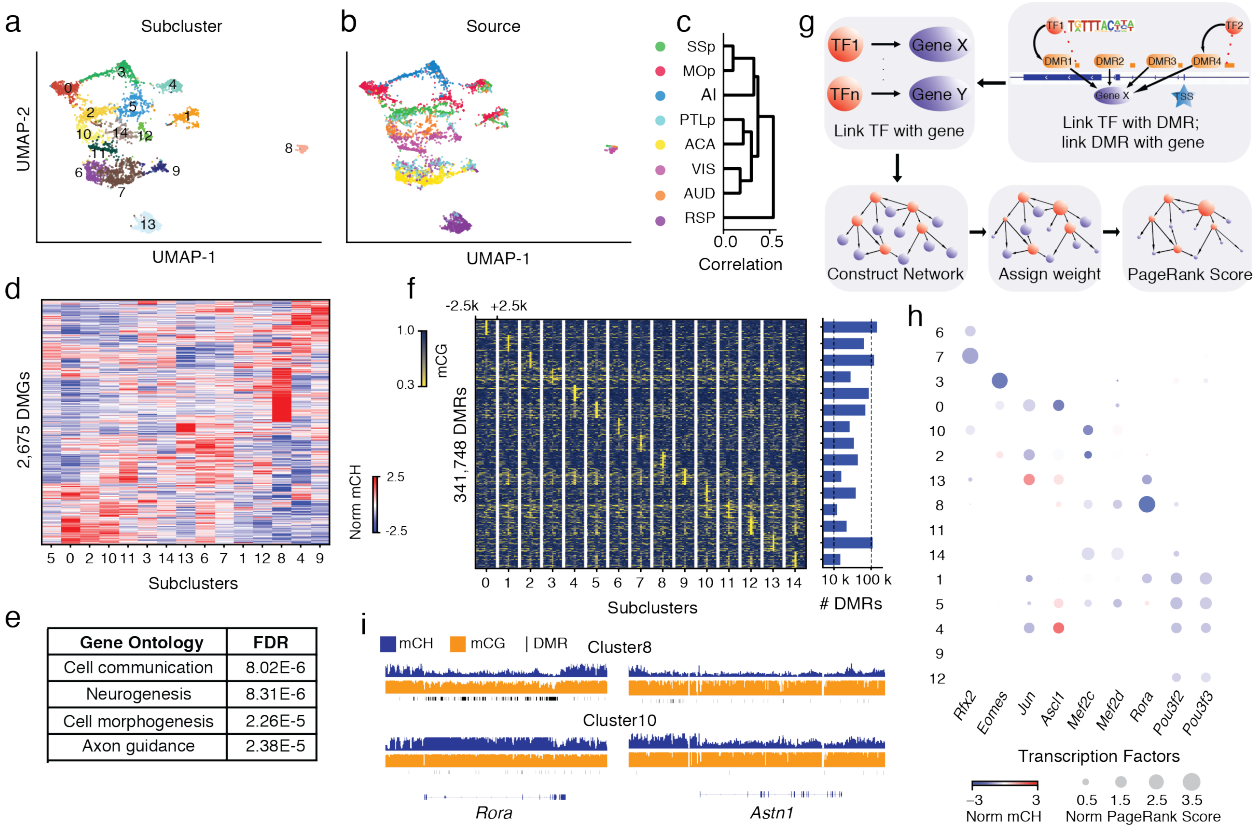

Fig. 3 Epigenetic diversity of L5-ET neurons.

a, b, Fifteen subclusters of L5-ET neurons (n=4,176) were identified and visualized on the uniform manifold approximation and projection (UMAP) plot generated using mCH levels in 100 kb genomic bins, colored by cluster (**a**), or the source region of neurons (**b**). **c**, Dendrogram shows the similarities between mCH profiles of L5-ET neurons from different source regions. **d, e**, In total, 2,675 CH-DMGs were identified in pairwise comparisons between L5-ET subclusters. Gene body mCH levels in each subcluster were visualized in the heatmap (**d**). Gene ontology (GO) enrichment of the CH-DMGs (**e**). **f**, Analysis of CG methylation (mCG) identified 341,748 differentially methylated regions (CG-DMRs) across the 15 L5-ET subclusters. The mCG levels at CG-DMRs and their 5kb flanking genomic regions in each subcluster were visualized in the heatmap (left). The numbers of CG-DMRs hypo-methylated in each subcluster were plotted in the bar chart (right). **g**, Workflow of the PageRank algorithm to infer crucial transcription factors. **h**,

563 Examples of some predicted key regulator TFs are shown in the bubble plot. The size of each dot
564 represents the normalized PageRank score of the TF. The color of the dot represents the gene body
565 mCH of the TF in the corresponding L5-ET subcluster. **i**, Browser tracks of mCH (blue), mCG
566 (orange), and CG-DMRs (black ticks) at *Rora* and its predicted gene target *Astn1*.
567

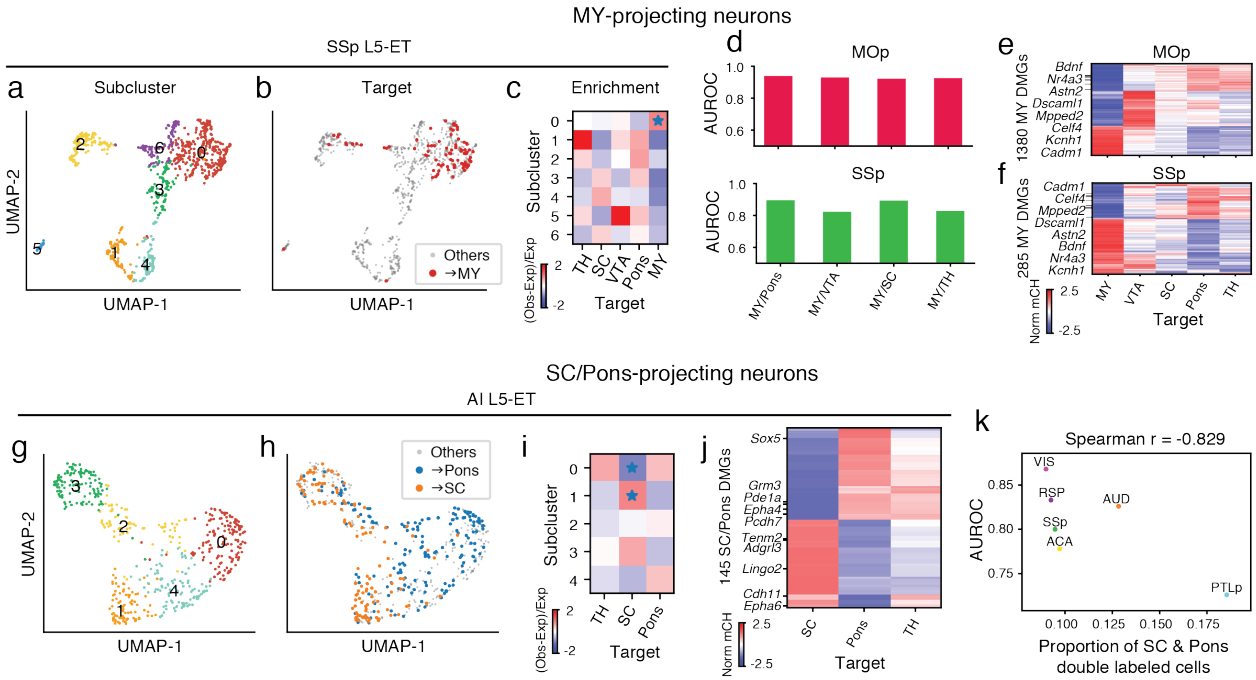

Fig. 4 Epigenetic differences between L5-ET neurons projecting to different targets. **a-f**, L5-ET neurons projecting to MY had more distinct DNA methylation profiles than other L5-ET neurons: SSp L5-ET neurons (n=884) segregated into 7 subclusters as visualized on the UMAP plot generated using mCH levels in 100 kb genomic bins (**a**). Compared to other SSp L5-ET neurons, SSp→MY neurons occupied a distinct space on the UMAP that corresponded to SSp subcluster 0 (**b**). The enrichment of SSp→MY neurons in SSp subclusters was calculated and visualized in the heatmap (**c**; * represents FDR<0.05). We constructed prediction models to distinguish →MY neurons from →Pons, →VTA, →SC, and →TH neurons. AUROC scores showed that the models performed well in both MOp (**d**, top) and SSp (**d**, bottom) for comparisons between →MY neurons versus neurons projecting to each of the other targets. **e, f**, In total 1,380 CH-DMGs were identified in pairwise comparisons between MOp→MY neurons and MOp neurons projecting to another subcortical ET target. The gene body mCH levels of these CH-DMGs in MOp neurons projecting to each ET target were visualized in the heatmap (**e**). Similarly,

285 SSp→MY CH-DMGs were identified and plotted in the heatmap (**f**). Gene names for example CH-DMGs that were hypo-methylated in both MOp→MY and SSp→MY neurons are highlighted in the heatmaps (**e, f**). **g-k**, Epigenetic differences between Pons-projecting versus SC-projecting neurons varied across cortical regions: In AI, L5-ET neurons (n=531) separated into 5 subclusters as visualized on the UMAP plot (**g**). AI→Pons and AI→SC neurons occupied different positions on the UMAP (**h**), corresponding to their differential enrichment in AI subclusters 0 and 1 (**i**; * indicating FDR<0.05). 145 CH-DMGs were identified between AI→SC versus AI→Pons neurons. mCH levels of these SC/Pons CH-DMGs in AI→SC, →Pons, and →TH neurons were plotted in the heatmap (**j**). **k**, The variation of AUROC from prediction models to distinguish →SC versus →Pons neurons from different source regions suggested that the levels of distinction between →SC and →Pons neurons vary between cortical regions. From this observation, we hypothesized that different cortical regions had different proportions of neurons that made dual projections to both SC and Pons. The proportion of double labeled cells was negatively correlated with the AUROC score in each source area, supporting the hypothesis.

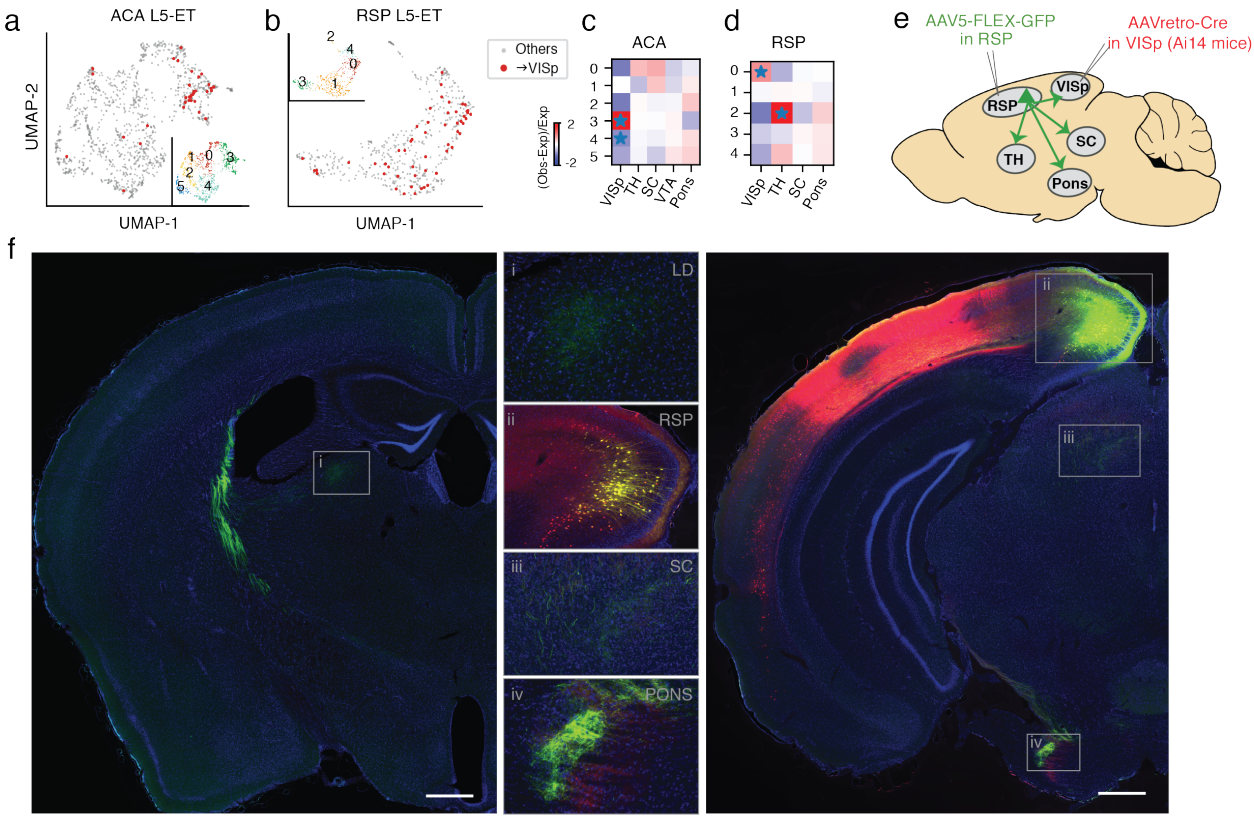

Fig. 5 A L5-ET neuron type that projects to both ET and cortical targets (L5-ET+CC). **a**, UMAP embedding of ACA L5-ET neurons (n=1,131) using mCH in 100 kb bins, colored by projection targets (ACA→VISp in red, n=36) and subclusters (Inset). **b**, UMAP embedding of RSP L5-ET neurons (n=516) using mCH in 100 kb bins, colored by projection targets (RSP→VISp in red, n=53) and subclusters (Inset). **c-d**, ACA→VISp neurons were enriched in ACA L5-ET subcluster 3 and depleted from subcluster 4 (**c**). RSP→VISp neurons were enriched in RSP L5-ET subcluster 0 (**d**). (* indicating FDR<0.05). These observations suggested that some ACA and RSP neurons project to both ET and cortical targets (L5-ET+CC). To validate the existence of this L5-ET+CC cell type, we designed an anatomical labeling experiment as illustrated in **e**. AAVretro-Cre was injected into VISp of Ai14 (Cre-dependent TdTomato) mice, and AAV5-FLEX-GFP (Cre-dependent GFP) was injected in RSP. Therefore, RSP→VISp neurons, including their axonal projections, were selectively labeled with GFP. If RSP→VISp neurons also project to ET targets

610 (L5-ET+CC neurons exist), GFP-labeled axons would be expected in subcortical ET targets such
611 as SC, Pons, and TH. **f**, We performed these labeling experiments in three Ai14 mice and observed
612 the same result in all mice. Examples of brain sections from one animal are shown. VISp neurons
613 at the AAVretro-Cre injection site were labeled by tdTomato (red). RSP→VISp neurons were
614 labeled with GFP (green), among which RSP→VISp neurons at the AAV5-FLEX-GFP injection
615 site were labeled with both tdTomato and GFP (yellow; inset ii). Strong GFP signals of
616 RSP→VISp axon terminals in subcortical ET regions were observed, including in the laterodorsal
617 (LD) nucleus of the thalamus (inset i), SC (inset iii), and Pons (inset iv). Scale bars: 500 μm (low
618 magnification).
619

620 **Methods**

621 **Experimental Animals.**

622 All experimental procedures using live animals were approved by the Salk Institute Animal Care
623 and Use Committee. The knock-in mouse line, R26R-CAG-loxp-stop-loxp-Sun1-sfGFP-Myc
624 (INTACT) was used for most experiments[4] and they were maintained on a C57BL/6J background.
625 42-49 day old adult male and female INTACT mice were used for the retrograde labeling
626 experiment. Adult C57BL/6J "wild-type" mice were used for double-retrograde labeling
627 experiments.

628

629 **Surgical Procedures for Viral Vector and Tracer Injections.**

630 To label neurons projecting to regions of interest, injections of rAAV2-retro-Cre (produced by
631 Salk Vector Core or Vigene, $2x10^{12}$ to $1x10^{13}$ viral genomes/ml, produced with capsid from
632 Addgene plasmid #81070 packaging pAAV-EF1a-Cre from Addgene plasmid #55636) were made
633 into both hemispheres of the INTACT mice. Animals were anesthetized with either
634 ketamine/xylazine or isoflurane, placed in a stereotaxic frame, and 0.1 to 0.5 microliters of AAV
635 was injected by pressure into stereotaxic coordinates corresponding to the desired projection target.
636 A list of injection coordinates and volumes is provided in Supplementary Table 1. At least 2 male
637 and 2 female mice were injected for each projection target. To label RSP neurons that project to
638 VISp, RSP was injected with rAAV2-retro-Cre and VISp was injected with AAV-FLEX-GFP
639 (Salk Vector Core) in each of 3 adult, Ai14 mice.

640

641 **Assessment of Double-Retrograde Labeling.**

642 To assess double-labeling of cortical cells projecting to Pons and/or Superior Colliculus,
643 stereotaxic pressure injections of 0.1-0.2 microliters of 0.25-0.5% of Cholera Toxin Subunit B
644 (CTB), Alexa Fluor 488 or 647 conjugated (Molecular Probes), were made into the pons and into
645 SC of 4 mice. 6-7 days later, animals were perfused with phosphate buffered saline (PBS) followed
646 by 4% paraformaldehyde in PBS. Brains were removed and sectioned coronally at 40 microns
647 thickness with a freezing microtome. Sections were mounted and imaged with a 20X
648 epifluorescence objective and images assessed to identify single and double-labeled neurons that
649 were assigned to cortical areas. Only neurons in regions where labeled cells from both injections
650 overlapped were counted. Therefore, some cortical areas in which there was no overlap are not
651 included. For each animal, double labeled cells were quantified for each region as the proportion
652 of double-labeled divided by the sum of all labeled cells. Mean values from the 4 animals are
653 plotted in Fig. 4k.

654

655 **Brain dissection.**

656 Approximately two weeks after the AAVretro injection, brains were extracted from the 56-63 day
657 old INTACT mice, immediately submerged in ice-cold slicing buffer (2.5mM KCl, 0.5mM $CaCl_2$,
658 7mM $MgCl_2$, 1.25mM NaH_2PO4, 110mM sucrose, 10mM glucose and 25mM $NaHCO_3$) that was
659 bubbled with carbogen, and sliced into 0.6 mm coronal sections starting from the frontal pole.
660 From each AAVretro-injected brain, the slices were kept in the ice-cold dissection buffer from
661 which selected brain regions (Supplementary Table 1) were manually dissected under a fluorescent
662 dissecting microscope (Olympus SZX16), following the Allen Mouse Common Coordinate

663 Framework (CCF), Reference Atlas, Version 3 (2015) (Extended Data Fig. 1). The dissected brain
664 tissues were transferred to prelabeled microcentrifuge tubes, immediately frozen in dry ice, and
665 subsequently stored at -80ºC.
666
667 **Nuclei preparation and single-nucleus isolation.**
668 For each dissected brain region, samples from 2 males and 2 females were pooled separately as
669 biological replicates for nuclei preparation. The 2-mL glass tissue dounce homogenizer and pestles
670 (Sigma-Aldrich D8938-1SET) were pre-chilled on ice. Nuclei were prepared using a modified
671 protocol as reported by Lacar et al., 2016[25]. In summary, the frozen brain tissues were transferred
672 to the dounce homogenizer with 1 mL ice-cold NIM buffer (0.25M sucrose, 25mM KCl, 5mM
673 $MgCl_2$, 10mM Tris-HCl (pH7.4), 1mM DTT (Sigma 646563), 10µl of protease inhibitor (Sigma
674 P8340)), with 0.1% Triton X-100 and 5µM Hoechst 33342 (Invitrogen H3570), and gently
675 homogenized on ice with the pestle 10-15 times. The homogenate was transferred to pre-chilled
676 microcentrifuge tubes and centrifuged at 1000 rcf for 8 min at 4ºC to pellet the nuclei. The pellet
677 was resuspended in 1 mL ice-cold NIM buffer, and again centrifuged at 1000 rcf for 8 min at 4ºC.
678 The pellet was then resuspended in 450 µL of ice-cold NSB buffer (0.25M sucrose, 5mM $MgCl_2$,
679 10mM Tris-HCl (pH7.4), 1mM DTT, 9ul of Protease inhibitor), and filtered through 40µM cell
680 strainer. The filtered nuclei suspension was incubated on ice for at least 30 minutes with 50µl of
681 nuclease-free BSA for at least 10 minutes, then incubated with GFP antibody, Alexa Fluor 488
682 (Invitrogen, A-21311) and anti-NeuN antibody (EMD Millipore MAB377) conjugated with Alexa
683 Fluor 647 (Invitrogen A20173). $GFP^+/NeuN^+$ single nuclei were isolated using fluorescence-
684 activated nuclei sorting (FANS) on a BD Influx sorter with 100µm nozzle, and sorted into 384-
685 well plates preloaded with 2µl of digestion buffer for snmC-seq2[15] (20 mL digestion buffer consists

686 of 10 mL M-digestion buffer (2×, Zymo D5021-9), 1 ml Proteinase K (20 mg, Zymo D3001-2-20),
687 9 mL water, and 10 µL unmethylated lambda DNA (100 pg/µL, Promega, D1521)). The collected
688 plates were incubated at 50ºC for 20 minutes then stored at -20 ºC.
689
690 **snmC-Seq2 library preparation.**
691 The bisulfite conversion and library preparation were performed following the detailed snmC-seq2
692 protocol as previously described[15]. The snmC-Seq2 libraries were sequenced on Illumina Novaseq
693 6000 using the S4 flow cell 2 x 150 bp mode.
694
695 **Reads processing and quality controls.**
696 We used the cemba-data pipeline to generate allc files from fastq files (cemba-data.rtfd.io), as
697 described in Luo et al[6]. Specifically, the fastq files were first demultiplexed into single cells and
698 trimmed of Illumina adaptors and 10 bp on both sides with Cutadapt[26]. The reads were mapped to
699 mm10 INTACT mouse genome using Bismark[27] with Bowtie2 aligner for each single end
700 separately. The reads with MAPQ smaller than 10 were excluded. Potential PCR duplicates were
701 removed with Picard MarkDuplicates. The reads from two ends were then merged to generate allc
702 files using call_methylated_sites function in methylpy[28]. The global mCCC level was used to
703 estimate the non-conversion rate of bisulfite treatment. The cells with less than 500 k non-clonal
704 reads or non-conversion rate greater than 1% were removed from further analysis.
705

706 **Methylation data processing.**

707 For each single cell, we computed the methylated CH (mc) and total CH (tc) basecalls of all 100
708 kb bins across the genome and all gene bodies annotated in GENCODE vM10[29]. The autosomal
709 bins that were covered by more than 100 basecalls in greater than 95% of cells were used for
710 further analysis. The autosomal genes that were covered by more than 100 basecalls in greater than
711 80% of cells were used for further analysis.

712

713 **Computing posterior methylation levels.**

714 For each cell, we calculated the mean (m) and variance (v) of the mCH level across the 100 kb
715 bins or genes. Then a beta distribution was fit for each cell i, where the parameters were then
716 estimated by

717 $$\alpha_i = m_i(\frac{m_i(1-m_i)}{v_i} - 1)$$

718 $$\beta_i = (1-m_i)(\frac{m_i(1-m_i)}{v_i} - 1)$$

719 We then calculated the posterior mCH of each bin by

720 $$ratio_{ij} = \frac{\alpha_i + mc_{ij}}{\alpha_i + \beta_i + tc_{ij}}$$

721 We normalized this rate by the cell's global mean methylation by

722 $$global_i = \frac{\alpha_i}{\alpha_i + \beta_i}$$

723 $$M_{ij} = \frac{ratio_{ij}}{global_i}$$

724 The values greater than 10 in M were set to 10. After normalization, M_{ij} is close to 1 when tc_{ij} is
725 close to 0.

726

727 **Identification of highly variable bins.**

728 Highly variable methylation features were selected based on a modified version of the
729 highly_variable_genes function in Scanpy[30]. In brief, since both the mean methylation level and
730 the mean coverage of a feature (100 kb bin or gene) can impact methylation level dispersion[6], we
731 grouped features that fall into a combined bin of mean and coverage, and then normalized the
732 dispersion within each group. After dispersion normalization, we selected the top 2,000 features
733 based on normalized dispersion for dimension reduction.

734

735 **Removing potential doublets.**

736 By plotting all cells on t-SNE, we noticed a cell population that was located in the center of the
737 plot and has a greater number of non-clonal reads than the others. To remove these potential
738 doublets, we modified scrublet[31] to adopt it to methylation data. Specifically, we first simulate the
739 doublet cells by randomly selecting two cells in our dataset and sum the methylation/total basecalls
740 of the two cells. Then the methylation levels of the simulated cells were computed using the
741 posterior computing method. We simulated twice the number of doublets as the number of real
742 cells. The top 2,000 highly variable features were selected for dimension reduction with principal
743 component analysis (PCA) and the top 50 PCs were used to train a k-nearest neighbor (kNN)
744 classifier (k=50) to predict a doublet score for each cell. Based on the histogram of doublet scores
745 of real and simulated doublet cells, the cells with doublet score higher than 0.1 were removed from
746 further analysis. After removing the potential doublets, 13,414 cells were kept for further analysis.

747

748 **Cell clustering and annotation.**

749 After removing potential doublets, the top 2,000 highly variable features were selected for
750 dimension reduction with PCA. The top 50 PCs were used for t-SNE visualization and construction
751 of kNN graph (G) with Euclidean distance (k=25). We use A to represent the connectivity of G,
752 where A_{ij} is 1 if node j is among the 25 nearest neighbors of node i, otherwise 0. The edge weights
753 of G were assigned as the jaccard distance of the connectivity matrix A. We ran Louvain clustering
754 (https://github.com/taynaud/python-louvain) with resolution 1.2 to partition the cells into 31
755 clusters and merged these clusters into major cell types based on known marker genes. The 11,827
756 cells within neuronal cell clusters were selected for further analysis.

757

758 **Neighbor enrichment score.**

759 The score was used to quantify the enrichment of cells that belong to the same category among the
760 neighbors of each cell. A higher score represents the cells are more likely to form clusters with the
761 cells belonging to the same category rather than in the other categories. The advantage of this score
762 is that it only considers the local effect so that would remain high if the cells in a category form
763 several different clusters that dissimilar with each other. The score was computed as follows.
764 Euclidean distances between each pair of cells were computed using the first 50 PCs. For each cell,
765 we found its 25 nearest neighbors in the same category, and $25r$ nearest neighbors from other
766 categories, where r is the ratio between total number of cells in other categories and total number
767 of cells in the same category. The area under the receiver operating characteristic (AUROC) using
768 distances between the cell and these neighbor cells for distinguishing the categories were defined

769 as the neighbor enrichment score of this cell. The methylation pattern of male and female mice are
770 highly similar on autosome; therefore, the two genders were treated as replicates in the analyses.
771
772 **Pairwise prediction of the source and target regions.**
773 Based on the sources, and targets, the neurons could be separated into groups. Each group contains
774 the neurons projecting from a specific source to a specific target. To test the similarity of two
775 groups of cells based on DNA methylation, we trained logistic regression models to predict the
776 group label of each cell. The posterior of 100 kb-bin or gene body mCH were used as features. We
777 split the cells into training and testing sets based on the gender of the mice where the cell came
778 from. The area under the receiver operating characteristic (AUROC) from cross-validation was
779 used to measure the performance of the model. The higher AUROC represents better ability of the
780 model to present the group label, which indicated the two groups had larger mCH differences and
781 were more distinguishable.
782 When the groups being studied contained cells from different clusters (e.g. cortical projecting
783 neurons in one source), we up-sampled the training set to make it better capture the group
784 differences rather than the differences of cell distributions across clusters. For example, when
785 comparing neurons projecting to two different cortical targets, the cluster composition differences
786 could make the model over-weight the features marking different clusters. To get rid of this bias,
787 we randomly repeated the neurons from the under-representing group and ensured the two groups
788 had the sample number of training samples in each cluster. The models were then trained and
789 tested in the same setting as mentioned above.

790 Several reasons could contribute to a low prediction performance. 1) Some neurons make
791 projections to several targets simultaneously. These could result in the neurons being captured by
792 multiple retrograde labeling experiments of different targets. It would be impossible to predict a
793 single label with our pairwise models for this type of neuron. 2) Some neurons project to different
794 target regions but have tiny epigenetic differences. 3) The epigenetic differences between neurons
795 projecting to different targets varies across replicates. In this study, male and female mice were
796 treated as biological replicates after removing sex chromosomes. Although methylation patterns
797 of autosomes are similar, differences between genders might still exist. 4) The contamination
798 levels of some projections are high, which make larger noise and hinder the models to capture real
799 signals. 5) The sample sizes of some projections are small, which make the learning more
800 challenging.

801 If the cross source/cluster predictions (described below) performed better than the within
802 source/cluster models, we would suspect that shared differences between neurons projecting to
803 different targets exist across sources/clusters, and the major reason for lower accuracies of within
804 source/cluster models might be 4) or 5) described above. To systematically distinguish 1) to 3),
805 other anatomic and genetic validation are still needed.

806

807 **Cross source prediction.**

808 The logistic regression models were trained to predict the projection targets in one source and
809 tested in the other source. The training set and testing set came from mice of different genders.
810 Specifically, the final AUROC were the average of AUROCs by training in male mice and testing

811 in female mice and by training in female mice and testing in male mice. For cortical targets, we
812 up-sampled the training set in the same way as the above section.
813
814 **Cross cluster prediction.**
815 This analysis was specifically for CC projection neurons to study whether the mCH differences
816 between projection neurons were shared or distinct across clusters (layers). The logistic regression
817 models were trained to predict the projection targets in one cluster and tested in the other cluster.
818 The training set and testing set came from mice of different genders.
819
820 **Identification of differentially CH-methylated genes (CH-DMGs).**
821 Wilcoxon rank-sum test and t test were widely used to identify differential genes in single-cell
822 studies[30], which consider each cell as an independent sample. However, the cells from the same
823 replicate, individual, or batch would be more similar than the cells from different ones. Therefore,
824 considering all cells as independent samples would overestimate the statistical power in single-
825 cell data. To address this problem and take the replicate-level variation into consideration, we used
826 a linear mixed model for the differential analysis and performed paired-wise comparisons between
827 groups. The posterior mCH level of 12,261 autosomal genes after coverage filters were used for
828 these analyses. The posterior gene-body mCH was used as dependent variables. Each individual
829 mouse was considered as a random effect. The global mCH levels and the gender of the mice were
830 considered as fixed effects. Other fixed effects were determined based on the comparison.
831 Specifically,
832 For DMGs between L5-ET clusters:

833 Gene_mCH ~ cluster + gender + global_mCH + (1 | mouse)

834 For DMGs between cortical targets in each source:

835 Gene_mCH ~ target + cluster + gender + global_mCH + (1 | mouse)

836 For DMGs between ET targets in each source:

837 Gene_mCH ~ target + gender + global_mCH + (1 | mouse)

838 Each gene was tested separately, and two-sided Wald test was performed to estimate the *P* value
839 for the effect being tested. FDR was computed for each pair of groups with the
840 Benjamini/Hochberg process. The fold-change of each gene was computed by the average mCH
841 across cells in one group divided by the average mCH across cells in the other group, with pseudo-
842 counts of 0.1. The criterions for significance when testing difference variables were distinct and
843 shown as follows. For DMGs between L5-ET clusters: absolute log fold-change greater than log1.5
844 and FDR smaller than 0.01. For DMGs between IT targets or between ET targets in each source:
845 absolute log fold-change greater than log 1.25 and FDR smaller than 0.01.

846

847 **Identification of differentially CG-methylated regions (CG-DMRs).**

848 To identify DMRs, we merged the allc files of individual cells assigned to the same cluster to
849 create a pseudo-bulk allc table for each cluster. Then we selected all the CG sites and combined
850 the methylation on two DNA strands for each CpG site. We run methylpy[28] DMRfind to identify
851 the DMRs and require the DMRs to contain at least 2 differentially methylated CpG sites (DMS).

852

853 **Inference of crucial transcription factors (TF) with PageRank.**

854 The method was modified from Taiji[19] to integrate the information of both gene body and
855 regulatory regions. The 537 motifs in JASPAR 2018 non-redundant core vertebrate database[32]
856 were used for these analyses. We scanned each of the motifs against the mm10 INTACT mouse
857 genome with ame[33] and *P* value cutoff as 1e-4. The DMRs between clusters were expanded 100
858 bp on both sides, and the ones overlapping with motifs were assigned to the corresponding TF.
859 The DMRs were also assigned to the potential genes they regulated using GREAT[34]. The TFs were
860 then linked with the target genes based on these DMRs that links to both the upstream TFs and the
861 downstream genes. A gene regulation network was constructed where the nodes represented the
862 genes and edges represented the links between TF genes and target genes.

863 To assign weights to the edges and initiate the node importance, the normalized $n_{cluster} \times n_{gene}$
864 methylation matrix (M) were min-max normalized across clusters to 0-1 by

865 $$N_{ij} = \frac{M_{ij} - min_{0<j'\leq n_{gene}} M_{ij'}}{max_{0<j'\leq n_{gene}} M_{ij'} - min_{0<j'\leq n_{gene}} M_{ij'}}$$

866 , and $1 - N_i$ were used as the predicted expression of each gene in cluster i. The predicted
867 expressions of all genes were used as starting importance I_0. Then we used a $n_{gene} \times n_{gene}$ matrix
868 A to represent the adjacency matrix of TF-gene regulation network, where A_{ij} was assigned as the
869 predicted expression level of gene i if gene i is a TF. To ensure an undirected propagation, we
870 used $B = A + A^T$ as the final adjacency matrix. B was normalized by row into the transition
871 matrix P by

872 $$P_{ij} = \frac{B_{ij}}{\sum_{j'=1}^{n_{gene}} B_{ij'}}$$

873 Next we performed a diffusion step of the PageRank scores through the network. For iteration t,

874 the PageRank scores were computed by

875 $$I_t = P \times I_{t-1} + rp \times I_0$$

876 , where rp represents a restart probability to balance the global and local effect of the propagation

877 on the network. The diffusion step was stopped when $|I_t - I_t| < 10^{-5}$.

878

879 **Clustering of L5-ET cells in each source region.**

880 L5-ET neurons from Epi-Retro-Seq and unbiased snmC-Seq were combined in this analysis. After

881 the same process as clustering all cells to derive posterior mCH level and select highly variable

882 features, the first 30 PCs were used for computing kNN (k=15) and Louvain clustering. The

883 resolutions used for source regions were 1.6 for MOp, AI, AUD, and RSP; 2.0 for SSp and PTLp;

884 1.0 for VISp; and 2.5 for ACA. The resolutions were determined based on visually examining the

885 cluster numbers and projection enrichment.

886 To confirm that there were epigenetic features distinguishing the clusters, we computed the

887 differentially methylated 100 kb bins (DMBs) across all pairs of subclusters using two-sided

888 Wilcoxon rank-sum test. The bins were defined as differential if the absolute log fold-change

889 between subclusters were greater than log 1.5, and FDR of the test smaller than 0.01. We also used

890 AUROC>0.85 and AUPR>0.6 to define DMBs, which provided similar results. Two subclusters

891 in RSP that had less than 5 DMBs were merged.

892

893 **Tests of projection enrichment in subclusters.**

894 As described above, the cells from the same replicate would be more similar, and considering all
895 cells as independent samples will overestimate the statistical power in single-cell data. Therefore,
896 we used linear mixed models to test for significant enrichment of particular projections in each
897 subcluster, considering the mouse where the cells came from. The subclsuter was used as
898 dependent variables. Each individual mouse was considered as a random effect. The projection
899 target was considered as fixed effects. [Subcluster ~ Target + (1 | mouse)]

900 Each projection target and each cluster were tested separately, and two-sided Wald test was
901 performed to estimate the *P* value for the effect being tested. FDR was computed for each source
902 with the Benjamini/Hochberg process. (Obs-Exp)/Exp in the enrichment matrices were computed
903 using the same method as in Pearson's chi-square test.

904

905 **Integration of Epi-Retro-Seq and Retro-Seq.**

906 Single-cell transcriptomic data from Tasic 2018[9,13] was downloaded from NCBI Gene Expression
907 Omnibus (GSE115746). 365 cells within clusters of 'L5 PT ALM *Npsr1*', 'L5 PT ALM *Slco2a1*',
908 and 'L5 PT ALM *Hpgd*' were selected for integration analysis. The raw data was preprocessed
909 using Scanpy[30]. Specifically, the read counts were normalized by the total read counts per cell and
910 log transformed. Top 10,000 highly variable genes were identified and z-score scaled across all
911 the cells. For methylation data, the posterior methylation levels of 12,261 genes in the 4,176 L5-
912 ET cells were z-score scaled across all the cells and used for integration. We used Scanorama[35] to
913 integrate the z-scored expression matrix and minus z-scored methylation matrix with sigma equal
914 to 100.

Overlap score.

Overlap score quantifies the similarity of the distributions of two groups of cells across clusters, where higher scores represent the two groups are more likely to be co-clustered. The scores were computed using the same method as in Hodge et al[14]. Specifically, a $n_{group} \times n_{cluster}$ matrix C was first computed, where C_{ik} represents the number of group i cells in cluster k. C was normalized by row to D, and the overlap score between group i and group j was defined as $\sum_{k=1}^{n_{cluster}} min(D_{ik}, D_{jk})$.

Data access and code availability

The data can be accessed via the NeMO ftp archive: http://data.nemoarchive.org/biccn/lab/callaway/projection/sncell/**.** The code for all of the analyses and the link to data browser can be found at https://github.com/zhoujt1994/Zhou2019.git

Author contribution

Contribution to research design: E.M.C., Z.Z, M.M.B., J.R.E., J.Z., X.J., K.L.

Contribution to data collection: Z.Z., Y.P., A.R., E.W., C.L., M.A.K., A.F., P.A.M, A.B, A.A., M.V., L.B., C.F., J.R.N., R.G.C., M.R., M.J., T.I., B.D., J.B.S, C.O., M.M.B.

Contribution to data analysis: J.Z., P.T, Z.Z., E.M.C, M.A.K, A.F., H.L., S.N.

Contribution to data archive/infrastructure: E.A.M., Z.Z., Y.P., A.R., A.B.

935 Contribution to research coordination: Z.Z., E.M.C., J.R.E., M.M.B., Y.P., X.J., E.W., C.L.,
936 E.A.M., K.L.
937 Contribution to writing manuscript: J.Z., Z.Z., E.M.C., P.T., J.R.E., E.A.M., M.M.B.
938

939 **Acknowledgements**

940 We thank Dr. Kai Zhang for advice on the PageRank algorithm, and Dr. Jesse R. Dixon for
941 insightful comments. We are grateful to Dr. Michael Nunn for help with management of the project.
942 This work is supported by NIMH U19MH114831 to E.M.C and J.R.E. M.A.K. is supported by
943 NEI F31 EY028853. The Flow Cytometry Core Facility of the Salk Institute is supported by
944 funding from NIH-NCI CCSG: P30 014195. J.R.E is an investigator of the Howard Hughes
945 Medical Institute.
946

947 **References**

948 1. Luo, L., Callaway, E. M. & Svoboda, K. Genetic dissection of neural circuits. *Neuron* **57**,
949 634–660 (2008).
950 2. Luo, L., Callaway, E. M. & Svoboda, K. Genetic Dissection of Neural Circuits: A Decade of
951 Progress. *Neuron* **98**, 256–281 (2018).
952 3. Mukamel, E. A. & Ngai, J. Perspectives on defining cell types in the brain. *Curr. Opin.*
953 *Neurobiol.* **56**, 61–68 (2019).
954 4. Mo, A. *et al.* Epigenomic Signatures of Neuronal Diversity in the Mammalian Brain. *Neuron*
955 **86**, 1369–1384 (2015).
956 5. Luo, C. *et al.* Single-cell methylomes identify neuronal subtypes and regulatory elements in

957 mammalian cortex. *Science* **357**, 600–604 (2017).

958 6. Luo, C. *et al.* Single nucleus multi-omics links human cortical cell regulatory genome
959 diversity to disease risk variants. *bioRxiv* 2019.12.11.873398 (2019)
960 doi:10.1101/2019.12.11.873398.

961 7. Lister, R. *et al.* Global epigenomic reconfiguration during mammalian brain development.
962 *Science* **341**, 1237905 (2013).

963 8. Price, A. J. *et al.* Divergent neuronal DNA methylation patterns across human cortical
964 development reveal critical periods and a unique role of CpH methylation. *Genome Biol.* **20**,
965 196 (2019).

966 9. Economo, M. N. *et al.* Distinct descending motor cortex pathways and their roles in
967 movement. *Nature* **563**, 79–84 (2018).

968 10. Chen, X. *et al.* High-Throughput Mapping of Long-Range Neuronal Projection Using In Situ
969 Sequencing. *Cell* **179**, 772–786.e19 (2019).

970 11. Klingler, E., Prados, J., Kebschull, J. M., Dayer, A. & Zador, A. M. Single-cell molecular
971 connectomics of intracortically-projecting neurons. *BioRxIV* (2018).

972 12. Kim, D.-W. *et al.* Multimodal Analysis of Cell Types in a Hypothalamic Node Controlling
973 Social Behavior. *Cell* **179**, 713–728.e17 (2019).

974 13. Tasic, B. *et al.* Shared and distinct transcriptomic cell types across neocortical areas. *Nature*
975 **563**, 72–78 (2018).

976 14. Hodge, R. D. *et al.* Conserved cell types with divergent features in human versus mouse
977 cortex. *Nature* **573**, 61–68 (2019).

978 15. Luo, C. *et al.* Robust single-cell DNA methylome profiling with snmC-seq2. *Nat. Commun.*
979 **9**, 3824 (2018).

980 16. Fejtova, A. *et al.* Dynein light chain regulates axonal trafficking and synaptic levels of
981 Bassoon. *J. Cell Biol.* **185**, 341–355 (2009).
982 17. Sanders, S. J. *et al.* Progress in Understanding and Treating SCN2A-Mediated Disorders.
983 *Trends Neurosci.* **41**, 442–456 (2018).
984 18. Zingg, B. *et al.* Neural networks of the mouse neocortex. *Cell* **156**, 1096–1111 (2014).
985 19. Zhang, K., Wang, M., Zhao, Y. & Wang, W. Taiji: System-level identification of key
986 transcription factors reveals transcriptional waves in mouse embryonic development. *Sci Adv*
987 **5**, eaav3262 (2019).
988 20. Harris, K. D. & Shepherd, G. M. G. The neocortical circuit: themes and variations. *Nat.*
989 *Neurosci.* **18**, 170–181 (2015).
990 21. Veinante, P. & Deschênes, M. Single-cell study of motor cortex projections to the barrel field
991 in rats. *J. Comp. Neurol.* **464**, 98–103 (2003).
992 22. Nelson, A. *et al.* A circuit for motor cortical modulation of auditory cortical activity. *J.*
993 *Neurosci.* **33**, 14342–14353 (2013).
994 23. Fries, W., Keizer, K. & Kuypers, H. G. Large layer VI cells in macaque striate cortex
995 (Meynert cells) project to both superior colliculus and prestriate visual area V5. *Exp. Brain*
996 *Res.* **58**, 613–616 (1985).
997 24. vogt Weisenhorn, D. M., Illing, R. B. & Spatz, W. B. Morphology and connections of neurons
998 in area 17 projecting to the extrastriate areas MT and 19DM and to the superior colliculus in
999 the monkey Callithrix jacchus. *J. Comp. Neurol.* **362**, 233–255 (1995).
1000 25. Lacar, B. *et al.* Nuclear RNA-seq of single neurons reveals molecular signatures of activation.
1001 *Nat. Commun.* **7**, 11022 (2016).
1002 26. Martin, M. Cutadapt removes adapter sequences from high-throughput sequencing reads.

1003 *EMBnet.journal* **17**, 10–12 (2011).

1004 27. Krueger, F. & Andrews, S. R. Bismark: a flexible aligner and methylation caller for Bisulfite-
1005 Seq applications. *Bioinformatics* **27**, 1571–1572 (2011).

1006 28. Schultz, M. D. *et al.* Human body epigenome maps reveal noncanonical DNA methylation
1007 variation. *Nature* **523**, 212–216 (2015).

1008 29. Frankish, A. *et al.* GENCODE reference annotation for the human and mouse genomes.
1009 *Nucleic Acids Res.* **47**, D766–D773 (2019).

1010 30. Wolf, F. A., Angerer, P. & Theis, F. J. SCANPY: large-scale single-cell gene expression data
1011 analysis. *Genome Biol.* **19**, 15 (2018).

1012 31. Wolock, S. L., Lopez, R. & Klein, A. M. Scrublet: Computational Identification of Cell
1013 Doublets in Single-Cell Transcriptomic Data. *Cell Syst* **8**, 281–291.e9 (2019).

1014 32. Khan, A. *et al.* JASPAR 2018: update of the open-access database of transcription factor
1015 binding profiles and its web framework. *Nucleic Acids Res.* **46**, D260–D266 (2018).

1016 33. Bailey, T. L., Johnson, J., Grant, C. E. & Noble, W. S. The MEME Suite. *Nucleic Acids Res.*
1017 **43**, W39–49 (2015).

1018 34. McLean, C. Y. *et al.* GREAT improves functional interpretation of cis-regulatory regions.
1019 *Nat. Biotechnol.* **28**, 495–501 (2010).

1020 35. Hie, B., Bryson, B. & Berger, B. Efficient integration of heterogeneous single-cell
1021 transcriptomes using Scanorama. *Nat. Biotechnol.* **37**, 685–691 (2019).

1022

Extended data figure legends

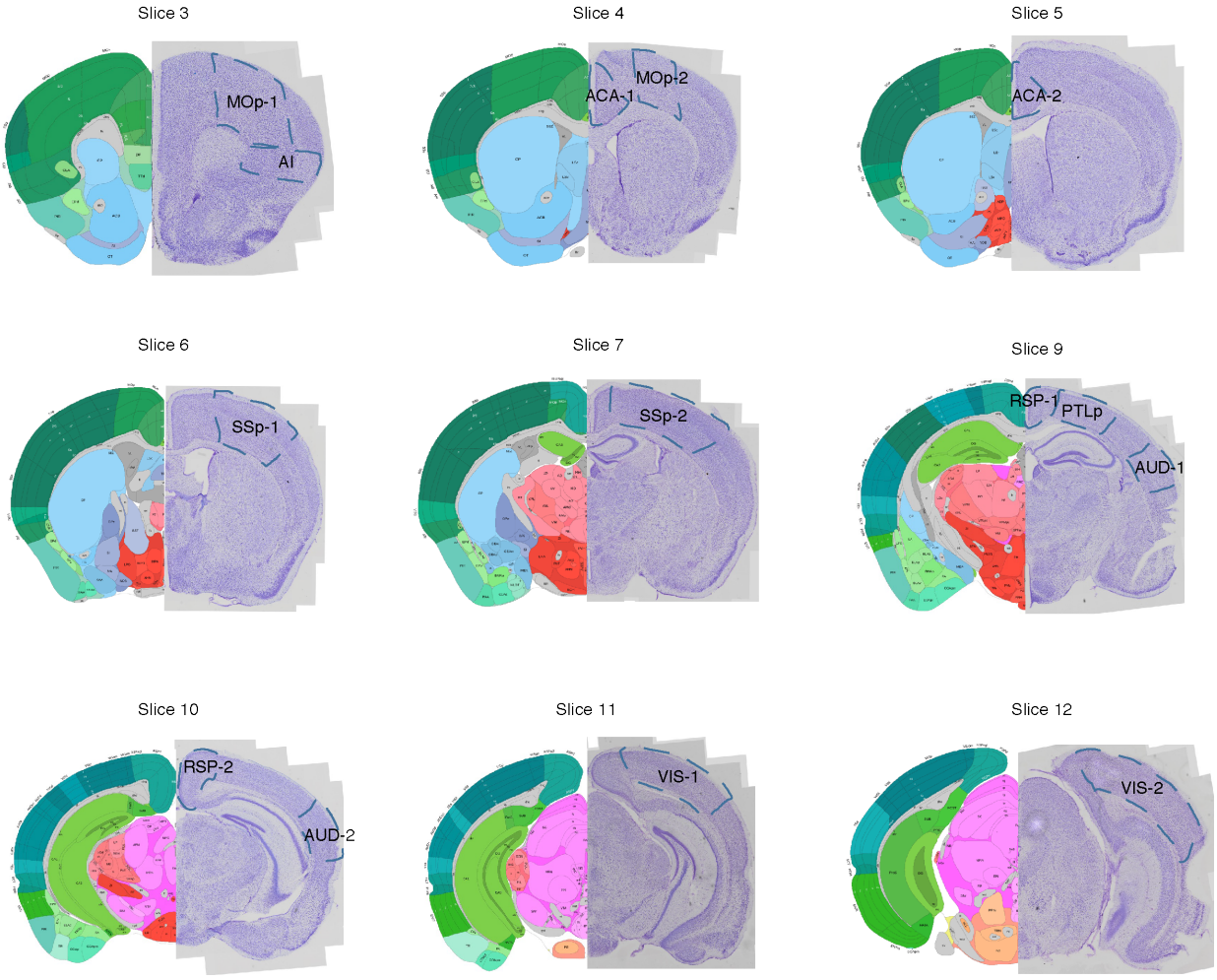

Extended Data Fig. 1 Source region dissection maps. The posterior views of dissected slices are shown. The slices correspond to Allen Reference Atlas level 33~39 (slice 3), 39~45 (slice 4), 45~51 (slice 5), 51~57 (slice 6), 57~63 (slice 7), 69~75 (slice 9), 75~81 (slice 10), 81~87 (slice 11), and 87~93 (slice 12), respectively.

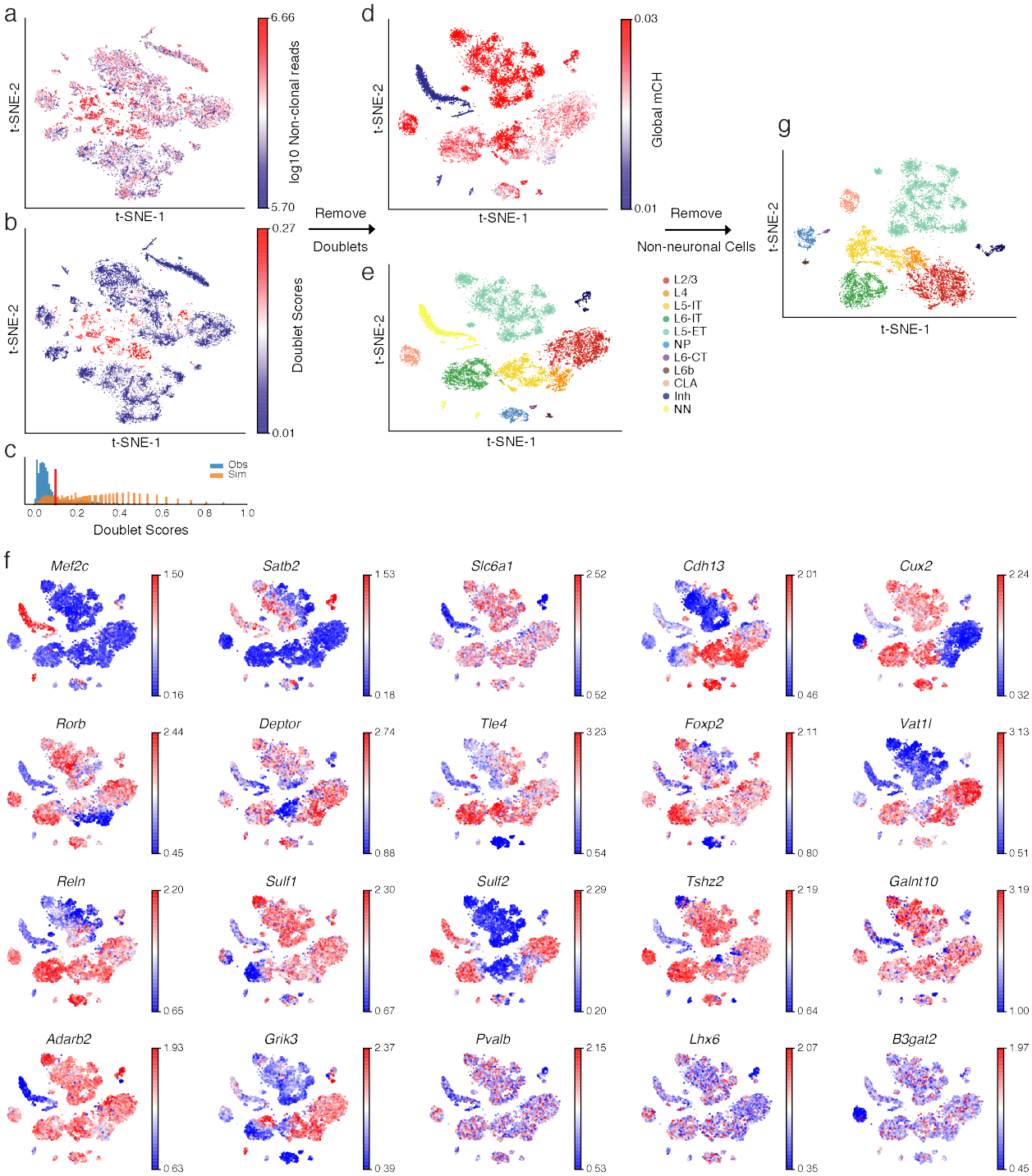

Extended Data Fig. 2 Removing potential doublets and non-neuronal cells. t-SNE of cells after quality control (n=16,971) colored by number of non-clonal reads (a) and predicted doublet scores (b). (c) Distribution of doublet scores for real cells (blue) and simulated doublets (orange). t-SNE of cells after removing doublets (n=13,414) colored by global mCH (d), cluster labels (e), and

1035 normalized gene-body mCH level of known cell type gene markers (f). Cells with low global mCH
1036 level are usually non-neuronal cells. t-SNE of single neurons (n=11,827) colored by the cluster
1037 labels (g). NN represents non-neuronal cells.
1038

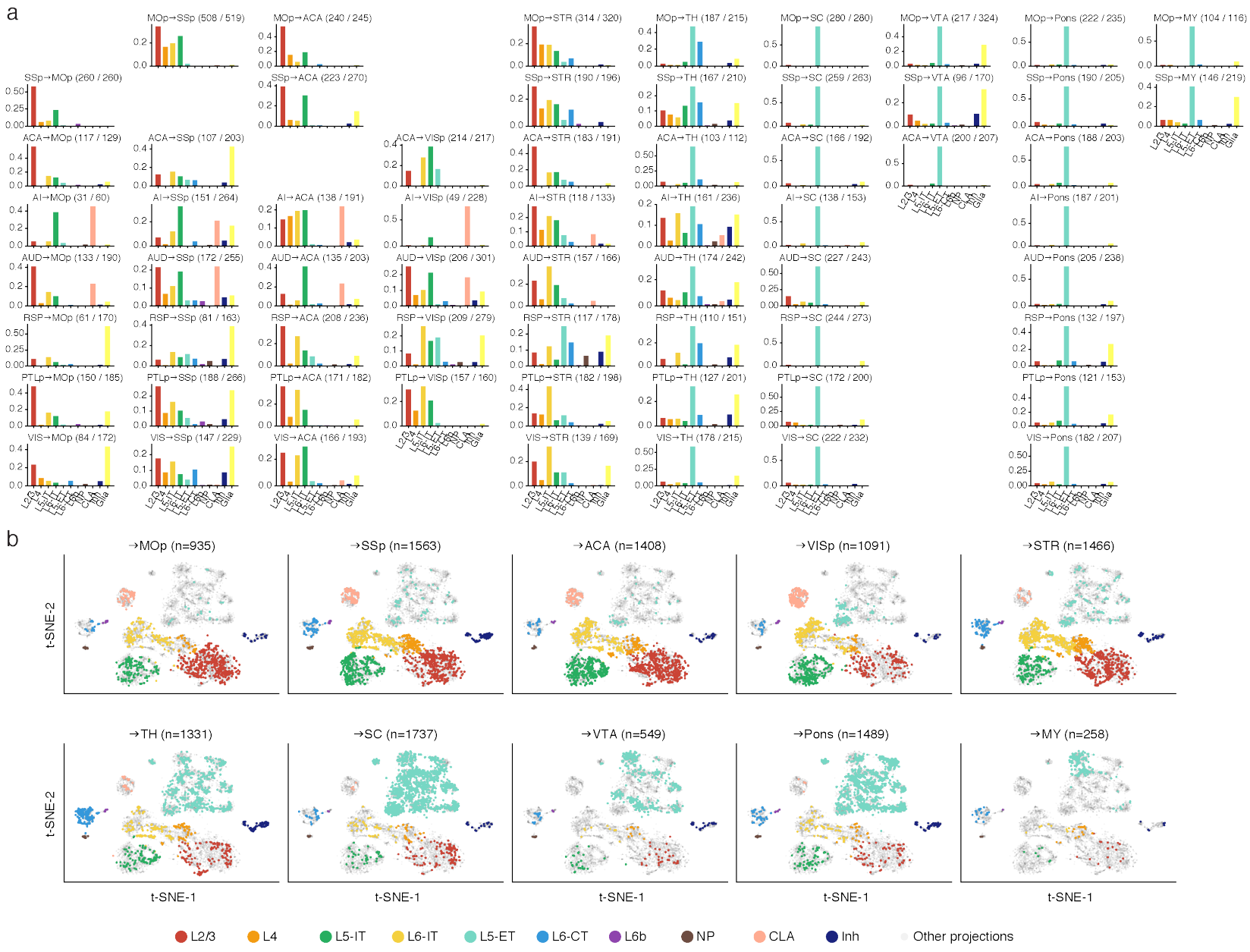
a
MOp→SSp (508 / 519)
MOp→ACA (240 / 245)
MOp→STR (314 / 320)
MOp→TH (187 / 215)
MOp→SC (280 / 280)
MOp→VTA (217 / 324)
MOp→Pons (222 / 235)
MOp→MY (104 / 116)
SSp→MOp (260 / 260)
SSp→ACA (223 / 270)
SSp→STR (190 / 196)
SSp→TH (167 / 210)
SSp→SC (259 / 263)
SSp→VTA (96 / 170)
SSp→Pons (190 / 205)
SSp→MY (146 / 219)
ACA→MOp (117 / 129)
ACA→SSp (107 / 203)
ACA→VISp (214 / 217)
ACA→STR (183 / 191)
ACA→TH (103 / 112)
ACA→SC (166 / 192)
ACA→VTA (200 / 207)
ACA→Pons (188 / 203)
AI→MOp (31 / 60)
AI→SSp (151 / 264)
AI→ACA (138 / 191)
AI→VISp (49 / 228)
AI→STR (118 / 133)
AI→TH (161 / 236)
AI→SC (138 / 153)
AI→Pons (187 / 201)
AUD→MOp (133 / 190)
AUD→SSp (172 / 255)
AUD→ACA (135 / 203)
AUD→VISp (206 / 301)
AUD→STR (157 / 166)
AUD→TH (174 / 242)
AUD→SC (227 / 243)
AUD→Pons (205 / 238)
RSP→MOp (61 / 170)
RSP→SSp (81 / 163)
RSP→ACA (208 / 236)
RSP→VISp (209 / 279)
RSP→STR (117 / 178)
RSP→TH (110 / 151)
RSP→SC (244 / 273)
RSP→Pons (132 / 197)
PTLp→MOp (150 / 185)
PTLp→SSp (188 / 266)
PTLp→ACA (171 / 182)
PTLp→VISp (157 / 160)
PTLp→STR (182 / 198)
PTLp→TH (127 / 201)
PTLp→SC (172 / 200)
PTLp→Pons (121 / 153)
VIS→MOp (84 / 172)
VIS→SSp (147 / 229)
VIS→ACA (166 / 193)
VIS→STR (139 / 169)
VIS→TH (178 / 215)
VIS→SC (222 / 232)
VIS→Pons (182 / 207)
L2/3 L4 L5-IT L6-IT L5-ET L6-CT L6b NP CLA Inh Glia
b
→MOp (n=935)
→SSp (n=1563)
→ACA (n=1408)
→VISp (n=1091)
→STR (n=1466)
→TH (n=1331)
→SC (n=1737)
→VTA (n=549)
→Pons (n=1489)
→MY (n=258)
t-SNE-2
t-SNE-1
L2/3
L4
L5-IT
L6-IT
L5-ET
L6-CT
L6b
NP
CLA
Inh
Other projections

1039

1040 **Extended Data Fig. 3 Cell type composition of all projections.** (a) The proportion of cells projecting from each source region (row)
1041 to each target region (column) in all clusters including non-neuronal cells. (b) t-SNE of neurons (n=11,827) projecting to each IT target
1042 (top) and ET target (bottom). The cells projecting to the target were colored by clusters and cells projecting to all other targets were
1043 greyed.
1044

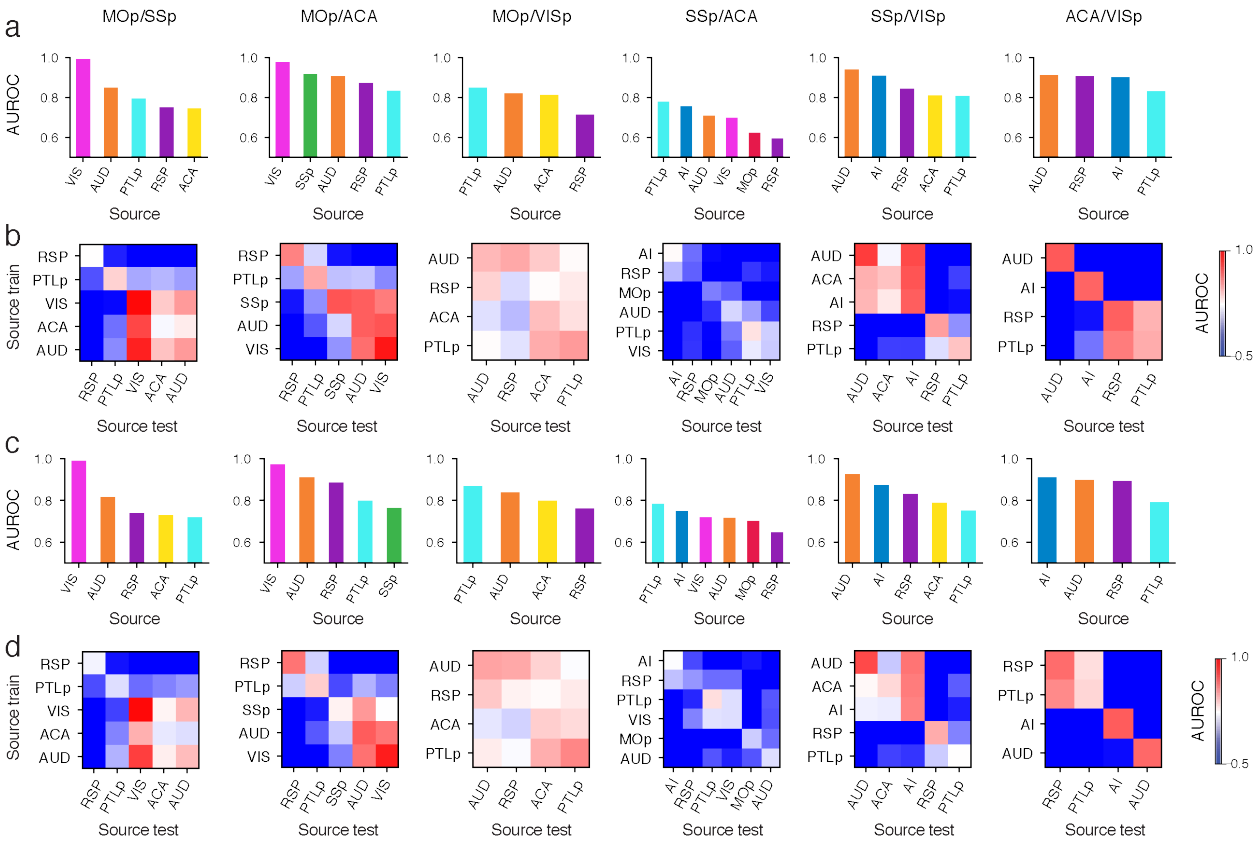

Extended Data Fig. 4 AUROC of cortical target pairs within and cross source regions. AUROC of models trained and tested in the same source region (a, c) or models tested in all source regions after trained in each one of them (b, d) using gene body (a, b) or 100 kb bin (c, d) mCH as features. The values in (a) and (c) correspond to the diagonals of (b) and (d) but ordered decreasingly.

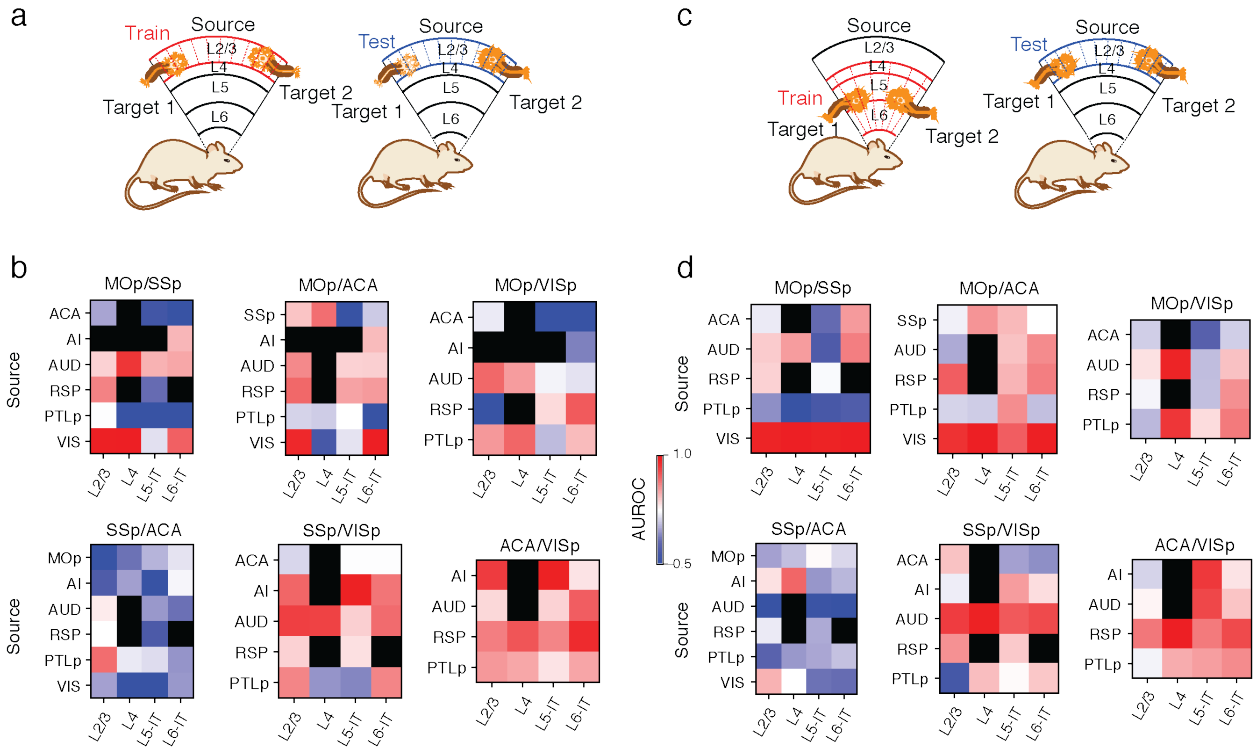

Extended Data Fig. 5 AUROC of cortical target pairs within and cross clusters. Demonstration of training and testing data for within layer prediction (a) and cross layer prediction (c). In (a), the models were trained and tested in the same layer with different replicates. In (c), the testing sets were the same as (a), but the models were trained in all other layers. AUROC of within layer prediction (b) or cross layer prediction (d). 100 kb-bin level mCH were used for all the predictions.

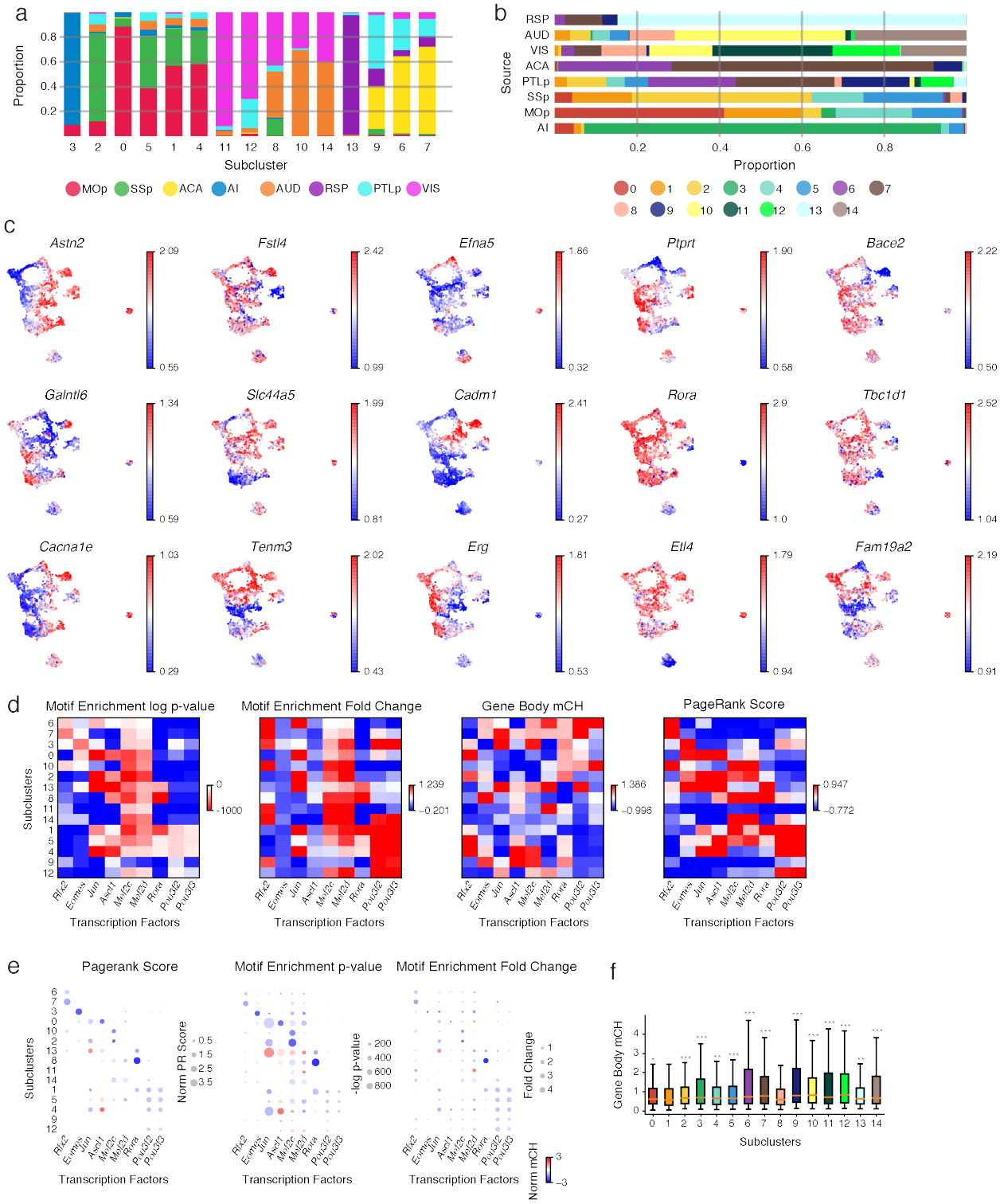

Extended Data Fig. 6 Signature genes and TFs of L5-ET subclusters. (a) Proportion of cells from all source regions in each subcluster. (b) Proportion of cells in all subclusters from each source region. (c) t-SNE of L5-ET cells (n=4,176) colored by the normalized gene-body mCH

level of subcluster gene markers. (d) Motif fold-change within DMRs, and motif enrichment *P* value within DMRs, gene-body mCH, and PageRank score of the example TFs in all L5-ET subclusters. (e) Gene body mCH (color) against PageRank score (size, left), motif enrichment *P* value (size, middle), and motif enrichment fold-change (size, right) for the example TFs in all L5-ET subclusters. (f) Gene body mCH in all clusters of *Rora* target genes identified in cluster 8. Significances were determined by comparing cluster 8 with each of the other clusters (two-sided Wilcoxon rank-sum test). * represents p<1e-2, ** represents p<1e-3, *** represent p<1e-4. The elements of all box-plots are defined as: center line, median; box limits, first and third quartiles; whiskers, 1.5× interquartile range.

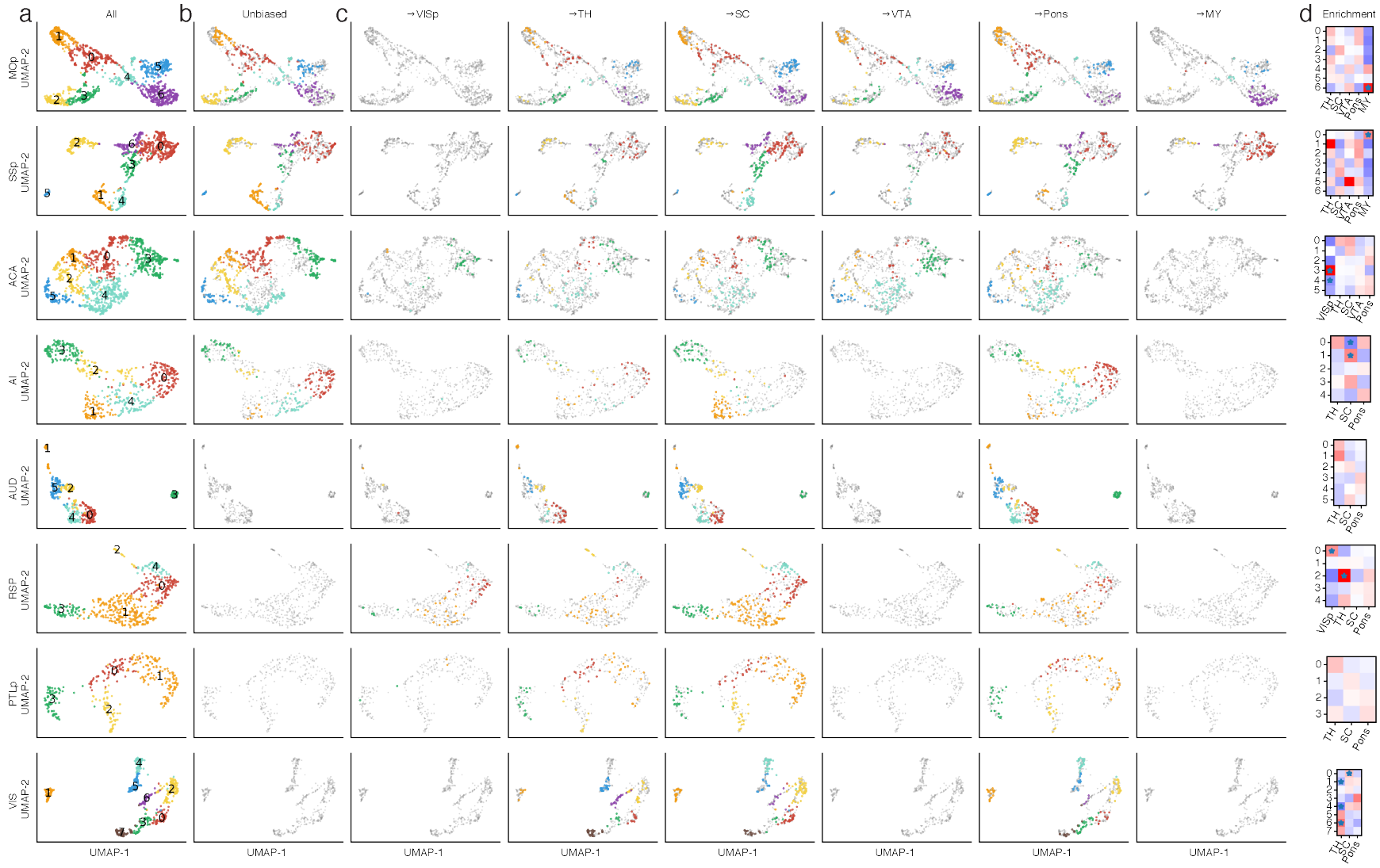

1074

1075 **Extended Data Fig. 7 Enrichment of different projections in L5-ET subclusters.** (a-c) t-SNE of L5-ET cells from each source region

1076 colored by subclusters. The colored cells are all cells (a), unbiased snmC-Seq cells (b), and cells projecting to each target (c). Other cells

1077 were greyed. (d) The enrichment of each projection in each L5-ET subcluster in each source. * represents FDR<0.05.

1078

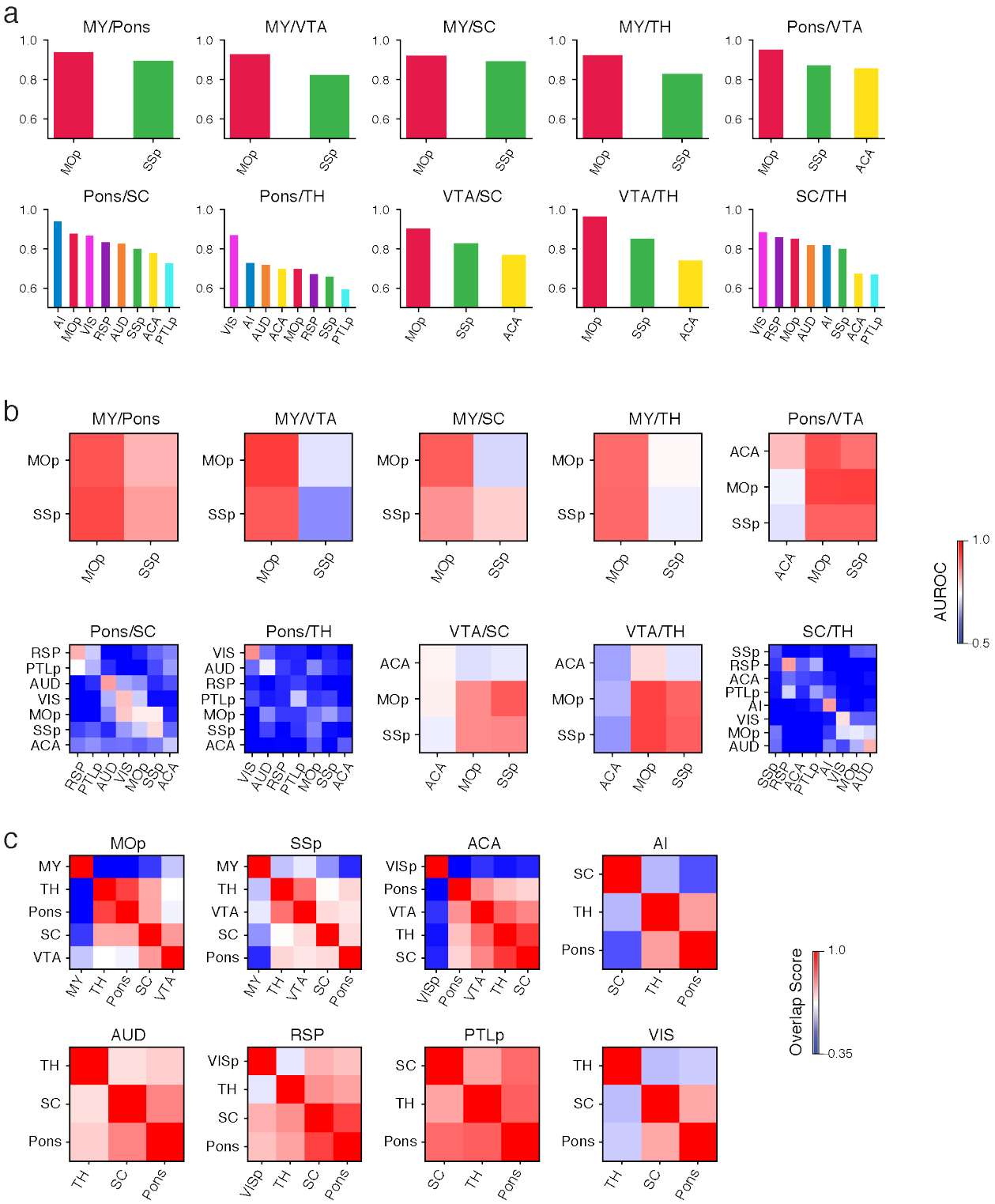

Extended Data Fig. 8 AUROC of ET target pairs within and cross source regions. AUROC of models trained and tested in the same source region (a) or models tested in all source regions

1082 after trained in each one of them (b) using 100 kb bin mCH as features. Training and testing sets
1083 were split by two-fold cross-validation in (a) to include AI, or split by replicates (b). (c) Overlap
1084 score between each pair of targets in each source region.
1085

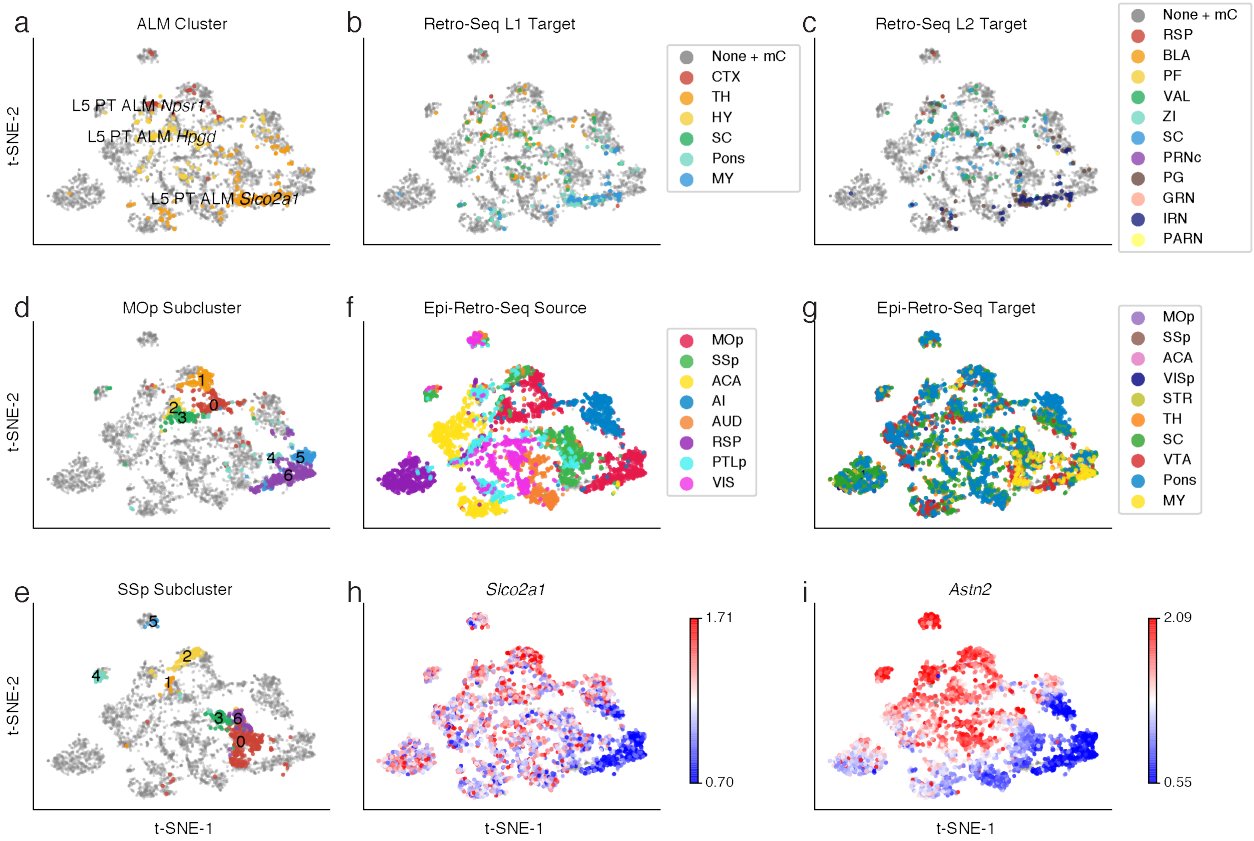

Extended Data Fig. 9 Integration of L5-ET cells from Epi-Retro-Seq and Epi-Seq. (a-c) L5-ET ALM cells in SMART-Seq (n=365) colored by clusters (a), major target regions (b), and detailed target regions (c). Epi-Retro-Seq cells were greyed. (d-i) L5-ET Epi-Retro-Seq cells from all source regions (n=4,176) colored by MOp subclusters (d), SSp subclusters (e), sources (f), targets (g), and gene body mCH of *Slco2a1* (h) and *Astn2* (i).

1093 **Supplementary Tables**

1094 **Supplementary Table 1. Epi-Retro-Seq injection information.**

1095 **Supplementary Table 2. Metadata and cluster assignment of 11,827 single neurons.**

1096 **Supplementary Table 3. CH-DMGs between IT neurons projecting to different target**

1097 **regions and GO enrichment.**

1098 **Supplementary Table 4. CH-DMGs between L5-ET subclusters and GO enrichment.**

1099 **Supplementary Table 5. CG-DMRs between L5-ET subclusters and target genes assigned by**

1100 **GREAT.**

1101 **Supplementary Table 6. CH-DMGs between L5-ET neurons projecting to different ET**

1102 **targets.**

1103 **Supplementary Table 7. Cell counting in double labeling experiments.**

1104